Accepted Manuscript

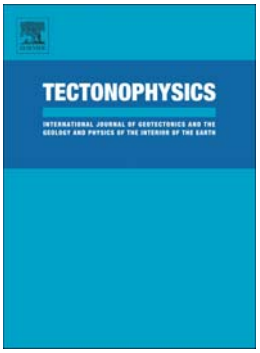

Middle–Late Holocene earthquake history of the Gyrtoni Fault, Central Greece: Insight from optically stimulated luminescence (OSL) dating and paleoseismology

Ioannis M. Tsodoulos, Konstantinos Stamoulis, Riccardo Caputo, Ioannis Koukouvelas, Alexandros Chatzipetros, Spyros Pavlides, Cristina Gallousi, Christina Papachristodoulou, Konstantinos Ioannides

PII: S0040-1951(16)30349-3
DOI: doi: 10.1016/j.tecto.2016.08.015
Reference: TECTO 127223

To appear in: *Tectonophysics*

Received date: 5 December 2015
Revised date: 18 August 2016
Accepted date: 21 August 2016

Please cite this article as: Tsodoulos, Ioannis M., Stamoulis, Konstantinos, Caputo, Riccardo, Koukouvelas, Ioannis, Chatzipetros, Alexandros, Pavlides, Spyros, Gallousi, Cristina, Papachristodoulou, Christina, Ioannides, Konstantinos, Middle–Late Holocene earthquake history of the Gyrtoni Fault, Central Greece: Insight from optically stimulated luminescence (OSL) dating and paleoseismology, *Tectonophysics* (2016), doi: 10.1016/j.tecto.2016.08.015

This is a PDF file of an unedited manuscript that has been accepted for publication. As a service to our customers we are providing this early version of the manuscript. The manuscript will undergo copyediting, typesetting, and review of the resulting proof before it is published in its final form. Please note that during the production process errors may be discovered which could affect the content, and all legal disclaimers that apply to the journal pertain.

ACCEPTED MANUSCRIPT

Middle-Late Holocene earthquake history of the Gyrtoni Fault, Central Greece: Insight from optically stimulated luminescence (OSL) dating and paleoseismology

Ioannis M. Tsodoulos [a, *], Konstantinos Stamoulis [a, b], Riccardo Caputo [c, d], Ioannis Koukouvelas [e, d], Alexandros Chatzipetros [f, d], Spyros Pavlides [f, d], Cristina Gallousi[a], Christina Papachristodoulou[a], Konstantinos Ioannides [a, b]

[a] *Department of Physics, University of Ioannina, GR-45110 Ioannina, Greece*

[b] *Archaeometry Center, University of Ioannina, GR-45110 Ioannina, Greece*

[c] *Department of Physics & Earth Sciences, University of Ferrara, I-44122 Ferrara, Italy*

[d] *Research and Teaching Center for Earthquake Geology, Tyrnavos, Greece*

[e] *Department of Geology, Division of Marine Geology and Geodynamics, University of Patras, GR-26500 Patras, Greece*

[f] *Department of Geology, Aristotle University of Thessaloniki, GR-54124 Thessaloniki, Greece*

ACCEPTED MANUSCRIPT

Abstract

The south-dipping Gyrtoni Fault defines the northeastern boundary of the Middle-Late Quaternary Tyrnavos Basin, Central Greece. The recognition and recent tectonic activity of the fault were previously based on mapping, remote sensing analyses and electrical resistivity tomography studies. To understand the Holocene seismotectonic behavior of the Gyrtoni Fault we excavated two paleoseismological trenches. To estimate the timing of past earthquakes using luminescence dating, we obtained twenty five fluvial-colluvial sediment and pottery samples from both the upthrown and the downthrown fault blocks. We applied the Optically Stimulated Luminescence (OSL) dating to coarse grain quartz using the single-aliquot regenerative-dose (SAR) protocol. Our investigations of luminescence characteristics using various tests confirmed the suitability of the material for OSL dating. We found that the estimated OSL ages were internally consistent and agreed well with the available

ACCEPTED MANUSCRIPT

stratigraphical data, archaeological evidence and radiocarbon dates. The performed paleoseismological analysis emphasized the occurrence of three surface faulting events in a time span between 1.42 ± 0.06 ka and 5.59 ± 0.13 ka. Also, we recognized an earlier faulting event (fourth) has been also recognized to be older than 5.59 ± 0.13 ka. The mean throw per event value of 0.50–0.60 m could correspond to a *ca.* M_w 6.5 earthquake. An average fault slip rate of 0.41 ± 0.01 mm/a and an average recurrence time of 1.39 ± 0.14 ka were also estimated. Our results suggest that the elapsed time from the most recent event (minimum age 1.42 ± 0.06 ka) is comparable with the mean return period.

*Keywords:*OSL (optically stimulated luminescence) dating; SAR; paleoseismology; Gyrtoni Fault; Central Greece

* Corresponding author.
E-mail address: itsodoul@cc.uoi.gr (I.M. Tsodoulos)

1. Introduction

In recent years, interest has increased in using paleoseismology to investigate the recent tectonic activity of small faults (10-20 km) with low slip rates (<1 mm/a) capable of producing moderate-to-strong linear morphogenic earthquakes (*sensu* Caputo, 2005) in intra-plate extensional systems of the broader Aegean region (e.g. Caputo et al., 2004; Caputo and Helly, 2005a; Chatzipetros et al., 2005; Vanneste et al., 2006; Kokkalas et al., 2007; Palyvos et al., 2010; Özkaymak et al., 2011; Moro et al., 2013; Zygouri et al., 2015; Galli et al., 2016; Grützner et al., 2016). Some of these faults were related to either historically or instrumentally recorded earthquakes and thus paleoseismological investigations extended the paleoseismic record further back in time. However, considerably less attention was given in faults located in regions with poor historic and low instrumental seismicity. Consequently, the study of these faults is then required for improving the seismic hazard assessment (Lafuente

ACCEPTED MANUSCRIPT

et al., 2011; Caputo et al., 2015), especially in densely populated areas (Zygouri et al., 2015; Grützner et al., 2016).

The Gyrtoni Fault (GF) is a south-dipping normal fault affecting Thessaly, Central Greece (Caputo, 1995; Pavlides et al., 2010), and is located ~13 km from Larissa, one of the largest cities of Greece with a population of ~163,000 (HSA, 2011) (Fig. 1). Therefore, the understanding of the seismotectonic behavior of this active fault in terms of slip rate, recurrence interval and date of past earthquakes (Keller and Pinter, 2002; McCalpin, 2009c), is of great importance considering that northern Thessaly may represent an important seismic gap within the broader Aegean Region (Caputo, 1995).

Previous palaeoseismological (Caputo et al., 2004; Caputo and Helly, 2005a), morphotectonic (Caputo, 1993a; 1993b), and geophysical studies (Caputo et al., 2003; Oliveto et al., 2004) as well as historical and instrumental records (Caputo and Helly, 2005b; Caputo et al., 2006) provide evidence for seismic activity along the major faults bordering the Tyrnavos Basin (Fig. 1a). Several large events have occurred in Thessaly during historical times and the instrumental period (Caputo and Helly, 2005b; Caputo et al., 2006 and references therein), but only three of these events have been directly related to the Tyrnavos Basin; the 1731 (M_s 6.0), the 1781 (M_s 6.3) and the 1941 (M_s 6.1) earthquakes (Galanopoulos, 1950; Papaioannou, 1988; Ambraseys and Jackson, 1990; Caputo, 1995; Papazachos and Papazachou, 1997) (Fig. 1a). Also, archaeological data, based on remains and damaged monuments, provide evidence of strong earthquakes in the Tyrnavos Basin during the last 2-3 ka (Caputo and Helly, 2005b). However, the correlation of these events with specific faults of Tyrnavos Basin and in particular with the GF is unknown.

Optically Stimulated Luminescence (OSL) dating (Huntley et al., 1985) provides age estimates for the last time a sediment was exposed to sunlight and it is a potentially useful tool in dating earthquake-related deposits (e.g. Porat et al., 1996; Chen et al., 2003; Fattahi et al., 2006; 2010). The single-aliquot regenerative-dose (SAR) protocol (Murray and Wintle, 2000; 2003) is extensively used for measuring the equivalent dose (D_e), providing a high degree of precision and accuracy for OSL ages (Murray and Olley, 2002; Rhodes et al., 2003;

ACCEPTED MANUSCRIPT

Murray and Funder, 2003) but also the multiple-aliquot regenerative-dose (MAR) protocol (Singhvi et al., 1982; Jain et al., 2003) has been applied in some cases.

A few previous studies have applied luminescence dating to fault-related deposits associated with paleoerthquakes, in Greece. Chatzipetros et al. (1998) were the first who applied thermoluminescence (TL) and ^{14}C dating to colluvial sediments associated with the Palaeochori-Sarakina Fault in western Macedonia, Greece, for estimating recurrence intervals of past earthquakes. In palaeoseismological investigations carried out along the Tyrnavos and the Rodia faults, Northern Thessaly, Caputo et al. (2004) and Caputo and Helly (2005a) reported TL, OSL and AMS ages from numerous trenches and estimated the co-seismic vertical displacement (throw), the recurrence interval between earthquake events, the slip rate, the elapsed time from the last earthquake and the maximum possible magnitude. Also in southwest Thessaly, across the Ekkara coseismic rupture associated with the 1954 Sophades earthquake, used OSL and infrared stimulated luminescence (IRSL) measurements were applied to the polymineral fine-grained fraction extracted from colluvial sediments to constrain the timing of past faulting events (Palyvos et al., 2010).

The present paper reports a paleoseismological and geochronological study of the GF in central Greece (Fig. 1a), where the recent tectonic activity was previously based on geological and geophysical techniques, like morphotectonic mapping, remote sensing analyses and electrical resistivity tomographies. In the present study, we aim at (1) shedding some light on the earthquake history of one of the major border faults of the Late Quaternary Tyrnavos Basin, (2) improving our knowledge on its seismogenic behavior, and (3) estimating its Holocene slip rate, average recurrence interval, maximum possible magnitude and the elapsed time from the last earthquake. In order to reach these objectives, we excavated two palaeoseismological trenches across the GF and following the detailed stratigraphic and structural logs, we collected numerous samples for an appropriate dating of event horizons. A major effort of this research was spent in the laboratory for the dating analyses. Ages have been obtained by systematically applying the OSL dating method using the SAR protocol

ACCEPTED MANUSCRIPT

(Murray and Wintle, 2000; 2003) allowing us to constrain the timing of the identified past surface faulting events.

2. Geological setting

The E-W trending GF along with the south-dipping Rodia Fault, to the north, and the antithetic Tyrnavos, Larissa and Asmaki faults, to the south, border and define the ~20 km wide and over 30 km long ESE-WNW oriented Tyrnavos Basin (Fig. 1a) (Caputo et al., 1994). This tectonic structure was developed during Middle-Late Pleistocene as a result of the roughly N-S lithospheric extension, which is still persisting in the area as indicated by the historical and instrumental records of seismicity (Caputo, 1990; Ambraseys and Jackson, 1990; Caputo and Pavlides, 1993; Papazachos and Papazachou, 1997).

The scarp marking the GF was initially described by Schneider (1968) as an important morphological feature (*Niederterrasse*) characterizing the northern Larissa Plain, but the occurrence of an active fault along the scarp was first suggested by Caputo (1990). The scarp length is around 13 km and is morphologically expressed as two right stepping en-enchelon segments (Fig. 1) (Caputo, 1995). The length of the western and eastern fault segments is about 7 and 5 km, respectively. Caputo et al. (1994) used geological, archaeological, historical and seismic data to suggest the recent tectonic activity of the GF. They also discussed the role of the GF during the Holocene palaeogeographic evolution of the Northern Larissa Plain.

The western segment of the GF offsets Late Pleistocene floodplain deposits (*Agia Sofia alluvium*, Schneider, 1968) in the footwall block, from Holocene alluvial deposits (*Gyrtoni alluvium*, Demitrack, 1986; van Andel et al., 1990). The morphological expression of the west fault segment is a south-facing ~12-m-high, wash-controlled, degraded fault escarpment (*sensu* Wallace, 1977). The scarp is visible on satellite images and aerial photographs as a slightly undulated feature (Fig. 1b). The western termination of this fault segment crosses the

ACCEPTED MANUSCRIPT

alluvial deposits of the Pinios floodplain, where the river displays a complex meandering pattern, with both abandoned and active meanders, near the fault scarp (Fig. 1b).

Based on neotectonic, morphotectonic and seismotectonic research a possible long-term slip rate lower than 0.1 mm/a was initially proposed for the GF (Caputo, 1995), thus ranking it as class C, according to the classification system of the Research Group of Active Faults of Japan (RGAFJ, 1992). Geophysical surveys were carried out by Caputo et al. (2003) and Oliveto et al. (2004) in order to document (1) the fault geometry at depth and (2) the approximate thickness and extent of the affected sedimentary layers. In particular, two parallel electric resistivity tomographies with 10 m of inter-electrode spacing where carried out across the western segment (Fig. 1b; Caputo et al., 2003), allowing locating the intersection of the fault plane with the scarp and its high-angle setting at least in the first 40-50 m (Fig. 2a). At a larger scale, Oliveto et al. (2004) applied the horizontal-to-vertical spectral ratios (HVSR) technique to estimate the differential sedimentary thickness across the major boundary faults of the Tyrnavos Basin. Regarding the GF, they reconstructed three profiles showing the likely continuity at depth of the fault and the important associated displacement. The results of the above geophysical investigations were crucial for selecting the trenching sites of the present research.

3. Materials and methods

3.1 *Paleoseismic investigation*

To define the paleoseismic activity of the GF, two single-slot (California-style) trenches were excavated across a 12-m-high, south-facing fault scarp at the central sector of the western segment of the GF (Fig. 1). The first trench (G1), dug in 2012 as an exploratory trench, and was 27 m-long, 2 m-wide and up to 4 m-deep. The second trench (G2) was 9 m-long, 2 m-wide and up to 3 m-deep, and was dug during 2014 at about 1 km to the west of the first trench. The walls of the trenches were cleaned, gridded with a 1 m by 1 m string grid, sedimentary boundaries and structural features were mapped in detail and photographed, and

ACCEPTED MANUSCRIPT

then samples were collected for age determination. The east wall of trench G1 is presented in Figure 3, while the east and west walls of the trench G2 are presented in Figures 4 and 5, respectively. Both trenches intersect the fault zone which separates a series of well stratified, thick to very thick beds of abandoned floodplain deposits exposed on the upthrown block, from fluvial and colluvial deposits on the downthrown block. The exposed sedimentary deposits are distinguished in units and labeled by numbers, whereas subunits are labeled with lower-case letters, based on their inferred age and stratigraphic position, as proposed by McCalpin (2009a). Although the exposed sedimentary units on both trenches are similar, the numbering of the units has been kept independent for each trench.

3.1.1 *Trench Gyrtoni 1 (G1)*

In this trench five lithostratigraphical units are distinguished in the upthrown block of the trench (units 1 to 5, Fig. 3). The bedding of the stratigraphic sequence of the upthrown block is slightly dipping towards the north by 3^{o} degrees. All unit boundaries are erosive and distinct in the exposed part of the upthrown block of the fault. A brief description of the exposed units is given below (from oldest to youngest). Unit 1 is a 2.4 m-thick, massive structureless, greenish-grey silty clay, with small scattered carbonate glaebules (caliche nodules) at the upper part of the unit. Unit 2, up to 1 m-thick, consists of discontinuous, wavy, non-parallel laminated to structureless greyish-black clay. At the boundary between the two units, a series of load and flame structures have been observed and interpreted as the result of the injection of the underlain silty clay sediments, of unit 1, to the clay sediments of unit 2. Unit 3 is a 50 cm-thick, crude parallel to sub-parallel laminated yellowish-grey silty clay, with well-developed caliche (carbonate) glaebules at the uppermost part of the unit. The sedimentological characteristics of units 1, 2 and 3 suggest overbank deposits accumulated on an alluvial plain. Additionally, the absence of well developed carbonaceous horizons on these units indicates a well-drained floodplain prone to episodic drying (Ghinassi et al., 2014). Unit 4, up to 90 cm-thick, and consists of moderately sorted, sub-rounded to sub-angular small pebbles, with a yellowish fine to very coarse sand matrix. The structure of the unit is

ACCEPTED MANUSCRIPT

characterized by well defined wavy to planar parallel bedding and bi-directional cross-lamination in the lower part. The facies analysis indicates that the sediments were deposited as channel-fill. Close to the NNE end of the trench, the channel is filled with massive silty sand. In the lowermost part of this unit, in some places, a very thin reddish sandy bed containing thin laminations of organic matter has been observed. Finally, unit 5 is a 30 cm-thick, discontinuous planar, non-parallel, bedded brownish-grey silty clay, with scattered angular granules to small pebbles.

On the downthrown block, two main units with a maximum exposed thickness of 2.3 m have been differentiated. Unit 6 is massive greyish-brown silty clay with scattered angular to sub-angular granules and small pebbles. Buried pottery found within unit 6 (21–22 m; Fig. 3), 2 m below the surface, was attributed possibly to the Middle Bronze Age (2000–1600 B.C.; Dr. A. Vlachopoulos, Department of History and Archaeology – University of Ioannina, pers. comm.). The upper part of this unit overlaps the lower fissure fill (unit f2, described later). Unit 7, up to 1 m thick, is massive greyish-brown silty clay with interspersed pottery fragments in the middle and the lower part of the unit. An erosional surface was observed at the boundary between units 6 and 7. The grain size, the massive structure and the lack or poor macroscopic stratification of both units suggest a floodplain environment characterized by repeated flooding events (van Andel et al., 1990) of an abandoned meander of the Pinios River, which flowed proximal to the Gyrtoni escarpment (Caputo et al., 1994). Close to the fault zone, units 6 and 7 may also contain some sedimentary contribution of colluvial origin from the upthrown block.

In the fault zone, we distinguished two fissure fills identified on the basis of change in color and texture (units f1 and f2, in Fig. 3) adjacent to the main fault. The older exposed fissure fill (unit f2) consists of structureless yellowish-grey silty-sand. Unit f1 corresponds to the younger exposed fissure fill in the fault zone and it consists of chaotic dark greyish clay with open cracks. The random fabric and the lithology of the filling material suggest deposition into the fissure of material derived mainly from unit 2, probably as a saturated mass (McCalpin, 2009b).

ACCEPTED MANUSCRIPT

All units described above are covered by a ploughed, laterally continuous brownish silty sand soil (unit 8), corresponding to the modern A horizon.

3.1.2 *Trench Gyrtoni 2 (G2)*

The stratigraphy of trench G2 is quite similar but not identical to that of trench G1. Figures 4 and 5 shows the lithological and structural logs of the east and the west trench wall, respectively. Due to the much shorter and shallower excavation across the upthrown fault block, only three lithostratigraphical units have been exposed (units 1 to 3). Unit 1 is the oldest exposed unit and it consists of discontinuous, planar and parallel bedded grey clay, progressively dipping to the south close to the fault zone. Unit 2 is a multi-storey palaeochannel belt up to 75 cm-thick. It is subdivided into sub-unit 2a, which corresponds to channel deposit, made up of well defined wavy to planar parallel bedded and south-directional cross-lamination, yellowish brown, fine to very coarse sand with sub-angular, moderately sorted, small pebbles. The sub-unit 2b is a lenticular structure of greyish silty-clay, probably a small size oxbow-lake deposit; and sub-unit 2c is the upper channel deposit, overlaying sub-units 2a and 2b, consisting of draped, parallel bedded yellowish brown medium to very coarse sand containing sub-rounded granules and shell fragments. At the boundary between unit 1 and sub-unit 2a, a load and flame structure was observed and interpreted as the result of differential sinking of the higher-density sand into the lower-density underlain clay (Fig. 4). The height of the flame structure reaches 30 cm. Unit 3 is an 85 cm-thick, crude parallel to sub-parallel laminated yellowish-grey silty-clay, with a thick calcrete horizon at the uppermost part of the unit, suggesting a well-developed soil profile. The calcrete horizon progressively bents towards the fault zone and is locally displaced. We interpreted unit 3 as a floodplain deposit.

On the downthrown block, two main sedimentary units were distinguished with a maximum exposed thickness of 3 m (Figs. 4 and 5). Unit 4 corresponds to a 60 cm-thick scarp derived colluvial deposit, composed of greenish grey silty-sand. Unit 5 is ~2.4 m thick, is greyish-brown massive silty-clay with scattered angular to sub-angular granules to small

ACCEPTED MANUSCRIPT

pebbles. Pottery fragments from different time periods i.e. 20th century BC to 15th century AD were found (Dr. Andreas Vlachopoulos, personal communication).

Similar to trench G1, we mapped two discrete fissure fills at the east wall of the trench, each corresponding to a surface-faulting earthquake (Fig. 4). Unit f2 corresponds to the older exposed fissure fill in the fault zone and consists of chaotic brownish silty-clay. The older fissure fill (f2) deposit was not detected at the west wall of the trench G2 (Fig. 5). The younger exposed fissure fill (unit f1) consists of structureless dark brownish silty-clay with open cracks.

A laterally continuous, ploughed, brownish silty sand soil with rare pebbles (unit 6 in Figs. 4 and 5) is developed on the upper part of the trench G2 and it corresponds to the modern A horizon.

3.1.3 *Deformation structures*

Both excavated trenches exposed a 2-m-wide fault zone composed of synthetic and antithetic normal fault strands. The secondary and the antithetic fault strands were merged to the main fault plane which turns into a single shear zone, dipping *ca.* 60^{o} to the south toward the base of the trenches (Figs. 3 - 5). Slickenlines were observed on the fault plane at the lower part of the east wall of trench G2, indicate a pure dip-slip movement. The fault zone is composed of displaced and dragged blocks of relatively intact and occasionally rotated (around 33^{o} down-to-the-south) sedimentary units from the up-thrown block (e.g. subunits 2a, 2b and 2c in Figs. 4 and 5), probably by frictional drag along the fault plane, and fissure fill deposits.

3.2 *Optically stimulated luminescence (OSL) dating*

3.2.1 *Sample collection*

In order to establish a reliable chronostratigraphic framework for this area and check the internal consistency, we collected several samples for OSL dating from the upthrown fault blocks of the two trenches. In particular, six samples were collected in trench G1 from four

ACCEPTED MANUSCRIPT

out of five of the recognized units (Fig. 3) and three samples were collected in trench G2 (Fig. 4).

On the other hand, for constraining the timing of the linear morphogenic earthquakes, eight sediment samples and five pottery fragments were collected from selected units outcropping in the downhrown fault blocks (Figs. 3, 4 and 5). Additionally, in trench G1 three samples were collected within the shear zone from blocks originally belonging to unit 5 and likely fallen within a co-seismic ground rupture during shaking (Fig. 3).

All sediment samples were collected by hammering 20 x 5 cm steel tubes horizontally into the surface of the walls of the two trenches. The tubes were closed and sealed using duct tape and aluminum foil, labeled and stored in black plastic bags. Samples for water content and dose rate determination were collected separately.

3.2.2 *Sample preparation*

Sample preparation and luminescence measurements were carried out at the luminescence dating laboratory of the Archaeometry Center at the University of Ioannina. The collected steel tubes were opened under subdued red light laboratory conditions. The outermost 2 cm of the sediment were removed from each end of the steel tubes to avoid contamination with light-exposed material and then the sediment from the central part of the cores was reserved for quartz OSL equivalent dose (D_e) determination. Pottery samples were sawed with a low speed diamond-impregnated wheel in order to remove a 2 mm layer from the surface and then were gently crushed and grinded using a vice and a mortar. Then quartz grains of 100-150 μm size were extracted by wet-sieving following the quartz inclusion technique (Aitken, 1985; Barnett, 2000; Polymeris et al., 2014). In respect to the sediment samples, the grain-size fraction of 125-250 μm, for samples from trench G1, and 63-100 μm, for samples from trench G2, were extracted by wet-sieving. The extracted grains were treated with 8% HCl and 30% H_2O_2 to remove carbonates and organic material. Finally, 40% HF was applied for 1 h to remove feldspars and to etch the outer surface of quartz grains, thus eliminating the alpha contribution, followed by concentrated HCl to remove any remaining

ACCEPTED MANUSCRIPT

soluble fluorides. After the chemical treatment, the grains were mounted on 10 mm diameter stainless steel discs by evaporation of an acetone suspension. The purity of the quartz extract was checked using the OSL-IR depletion ratio (Duller, 2003) and by observing the 110 °C TL peak during preheating (Constantin et al., 2014). The OSL-IR depletion ratio was added as an extra step within the SAR sequence to identify feldspar contamination in the samples. Aliquots with OSL-IR depletion ratio values within 10% of unity were accepted (Fig. 6).

3.2.3 *Equivalent dose determination*

Following sample preparation, luminescence measurements were performed on a Risø TL/OSL-DA-20 reader (Bøtter-Jensen et al., 2003; 2010) equipped with a 1.48 GBq ^{90}Sr-^{90}Y beta radiation source with a dose rate ~0.084 Gy/s. Quartz OSL was obtained through stimulating with blue LEDs emitting at 470 nm (FWHM = 20 nm) and delivering ~50 mW/cm^2 at the sample position and infrared (IR) stimulating using IR diodes emitting at 880 nm delivering ~145 mW/cm^2. Signals were detected using a 7 mm Hoya U-340 optical filter in front of an EMI 9235QA photomultiplier tube.

Measurements of OSL were made on chemically purified coarse-grained quartz, using the single-aliquot regenerative-dose (SAR) protocol (Table S1) proposed by Murray and Wintle (2000; 2003). All OSL measurements were made using stimulation with blue diodes at 125 °C for 40 s. To determine D_e, the initial 0.8 s (channels 1 to 5) of the OSL decay curve was used, and the background was assumed as the mean of the signal in the last 8 s (50 channels) of the 40 s measurement of the decay curve. Preheat temperatures of 240 ^{o}C for 10 s for sediment samples and 260 ^{o}C for 10 s for pottery samples, were chosen after performing preheat plateau tests (Fig. 7) and dose recovery tests (Fig. 8) using different preheat temperatures (see Section S1 for further details). A cut heat of 160 ^{o}C followed by immediate cooling prior to test dose response of approximately 5 Gy was used. Preliminary luminescence measurement tests on aliquots from the pottery samples, using the standard SAR protocol (Murray and Wintle, 2000), were found to have significant recuperated corrected OSL signal compared to the natural signal (e.g. GyrOSL1_13, >10%) (see Section

ACCEPTED MANUSCRIPT

S1 for further details). Thus, an additional 40 s optical stimulation at 280 ^{o}C (Murray and Wintle, 2003) was added at the end of each measurement cycle of the SAR protocol, and recuperation was reduced to <10% for all pottery samples. Dose-recovery tests have been performed on all samples (Wallinga et al., 2000; Murray and Wintle, 2003). Of 74 aliquots, ~85% had dose-recovery ratios within the range 0.9 - 1.1 (Fig. S1; see Section S1 for further details), confirming that the chosen SAR protocol is able to recover a given dose prior to any thermal treatment for all samples.

The aliquots measurements were accepted when the following criteria were satisfied: (i) recycling ratio of 1.0 ± 0.1 (Wallinga et al., 2000; Murray and Wintle, 2000), (ii) OSL-IR depletion ratio of 1.0 ± 0.1 (Duller, 2003), (iii) a detectable OSL signal (i.e. >3 sigma above background), (iv) recuperation of signal less than 5% of the natural signal (Murray and Wintle, 2000) for soil samples and 10% for pottery samples, and (v) whether the sensitivity corrected natural signal intersected the dose-response curve.

The D_e values were calculated using the Analyst software (v4.11; written by Duller, 2013; Duller, 2015) by fitting an exponential or exponential-plus-linear function to the dose-response curve, with an instrumental error of 1.0 % (Duller, 2007). Typical dose-response curves and natural OSL signal decay curves of characteristics samples are shown in Fig. 6 (see Section S1 for further details). The distribution of equivalent doses (Figs. S2 and S3) for each sample was then analyzed, using the R package numOSL (Peng et al., 2013) and displayed by a Radial Plot (v1.3; written by Olley, 2003). The central age model (CAM; Galbraith et al., 1999; Galbraith and Roberts, 2012) was applied to calculate the final D_e values for all samples (see Section S2 for further details). The estimated D_e values for all samples are summarized in Table 2.

3.2.4 *Dose rate assessment*

The environmental dose rate for each sample was calculated using high-resolution gamma spectrometry to measure the radionuclide concentrations of ^{238}U, ^{232}Th and ^{40}K (Murray et al., 1987), at the Nuclear Physics Laboratory of the University of Ioannina. Dry

ACCEPTED MANUSCRIPT

sample material was packed in plastic containers, sealed and stored at least for four weeks to allow for radon equilibrium before being measured on a Canberra broad energy HPGe gamma spectrometer for ~48 h. The concentrations of ^{238}U, ^{232}Th and ^{40}K were then used to calculate the dose rates using the conversion factors of Adamiec and Aitken (1998). The water content (% weight) of each sample was measured in the laboratory based on the initial field water content. In addition to the environmental dose rate, the contribution of the cosmic radiation was calculated based on the modern burial depth of the samples, the sediment density (1.8 g/cm^3) and the site's latitude, longitude and altitude, using the equations given by Prescott and Hutton (1994). The analytical results from gamma spectroscopy measurements are summarized in Table 1.

3.3 *Radiocarbon dating*

Samples for radiocarbon dating were collected from the two trenches and dated at the Center for Dating and Diagnostics, Department of Engineering for Innovation, University of Salento, Italy, using accelerator mass spectrometry (AMS) techniques. Charcoal and organic material collected from the exposed sediments of the trenches walls were used for dating. Radiocarbon dates were calibrated to calendar years using OxCal v3.10 (Bronk Ramsay, 1995; 2001) and the IntCal13 atmospheric curve (Reimer et al., 2013). Following Durcan et al. (2010) 64 years has been added to the radiocarbon dates, which are summarized in Figs. 3 - 5, in order to establish the same reference point as the luminescence ages (i.e. 2014 AD).

4. Results and discussion

4.1 *Trench chronostratigraphy*

The OSL ages were calculated by dividing the CAM D_e by the total dose rate. Table 2 summarizes the OSL ages obtained for the samples collected in the two excavated paleoseismological trenches across the GF. Corresponding ages are also reported in Figs. 3 to 5.

ACCEPTED MANUSCRIPT

The derived ages of the samples from the upthrown fault blocks of the two paleoseismological trenches are in stratigraphic order, within uncertainties (Figs. 3 and 4). The six samples from the exposed units on the upthrown block of trench G1 were dated between 46.1 ± 3.3 ka (unit 4) and 233.3 ± 12.5 ka (unit 1) (Table 2; Fig. 3). The ages of the three samples from the displaced blocks of unit 5 ranged from 20.9 ± 1.5 ka to 28.1 ± 2.1 ka (Table 2; Fig. 3), and are stratigraphically consistent. The OSL ages from the upthrown fault block clearly document that the excavated sediments were deposited during the upper part of the Middle Pleistocene and mainly during the Late Pleistocene. It is worth to note that units 4 and 5 range between 50 to 21 ka, in agreement with the age of c. 40 to 27 ka BP proposed by Van Andel et al. (1990) for the *Agia Sophia alluvium*, which is the most extensive unit of the *Niederterrasse*, deposited during the last glacial period, and presently covered by a mature paleosoil (*Agia Sophia soil*).

Three samples from the upthrown fault block of trench G2 provided ages of 92.6 ± 6.1 ka (Gyr2OSL_01E, unit 3), 96.9 ± 6.5 ka (Gyr2OSL_02E, unit 2a) and 148.2 ± 10.8 ka (Gyr2OSL_03E, unit 1). Sample Gyr2OSL_01E shows a comparable age (within one standard deviation) with sample Gyr1OSL_03 (86.4 ± 5.0 ka) which was taken from the middle part of the same silty-clay deposit (unit 3 in both trenches) of the trench G1 (Fig. 3 and 4). The sample Gyr2OSL_03E (148.2 ± 10.8 ka) collected from unit 1 is in stratigraphic order with the samples Gyr1OSL_05 (133.9 ± 5.5 ka) and Gyr1OSL_06 (233.3 ± 12.5 ka) taken from the upper and the lower part, respectively, of the same massive silty clay unit exposed on trench G1 (Figs. 3 and 4).

As concerns the downthrown fault block, a ceramic fragment (Gyr1OSL_15) from unit 6 (trench G1) provided an OSL age of 3.77 ± 0.13 ka (Table 2, Fig. 3). The pottery was estimated to be around 2000 – 1600 B.C. (Middle Bronze Age; Dr. Andreas Vlachopoulos, personal communication), and accords well with the OSL age. A sediment sample (Gyr1OSL_10) from the base of unit 7 (trench G1) provided an OSL age of 1.42 ± 0.06 ka (Table 2, Fig. 3). In stratigraphic agreement, the four pottery fragments from unit 7 (trench G1) provided OSL ages ranging from 1.98 ± 0.08 ka to 3.15 ± 0.13 ka (Table 2; Fig. 3).

ACCEPTED MANUSCRIPT

Similarly, in trench G2, the calculated OSL ages for unit 5 (east wall, Fig. 4) range from 1.35 ± 0.02 ka to 3.77 ± 0.06 ka (Table 2), while from the western wall of the same trench, a sediment sample (Gyr2OSL_01W) from the underlying unit 4 has provided an OSL age of 5.59 ± 0.13 ka (Table 2; Fig. 5). Overall, the calculated OSL ages indicate that the fluvial-colluvial deposits of the downthrown fault block were accumulated during the Middle-Late Holocene. In this regard, based on archaeological criteria previous researchers (Demitrack, 1986; van Andel and Zangger, 1990) proposed the *Gyrtoni alluvium*, covering the downthrown fault block, to have been deposited between c. 5.0 and 4.0 ka BP marking the end of the deposition of the higher floodplain of the Pinios River.

Independent age control was provided for two samples of trench G1 and one sample of trench G2 by radiocarbon dating. In trench G1 sample GyrC_{14}1_3 (1254 ± 30 yr BP) from the lower part of unit 7 provides a calibrated age of 1.24 ± 0.10 ka BP (2σ), which is in good agreement with the OSL age of sample Gyr1OSL_10 (1.42 ± 0.06 ka) (Fig. 3). Sample GyrC_{14}1_4 (2884 ± 35 yr BP) comes from the inside of the buried pottery found in unit 6 (subunit 6a) of trench G1 (Fig. 3) and consists of small charcoal fragments that provided a calibrated age of 2.62 ± 0.18 ka BP (2σ). The slight difference in age with respect to the OSL dated pottery fragment (Gyr1OSL_15; 3.77 ±0.13 ka) could be possibly due to the infilling of younger material within the artifact during a subsequent sedimentary and/or deformation event.

Finally, sample GyrC_{14}2_1 (2763 ± 45 yr BP) was collected from a buried pit with organic material found in unit 4 (trench G2, west wall; Fig. 5) providing a calibrated age of 2.92 ± 0.10 ka BP (2σ). The calibrated bulk ^{14}C age of this sample and that calculated with the OSL technique from sample Gyr2OSL_01W (5.59 ± 0.13 ka) are in stratigraphic order and the *ca.* 2.5 ka of age difference is likely due to radiocarbon underestimation, because ^{14}C dating of bulk organic material may produce ages reflecting the average carbon storage time, instead of the expected age (Trumbore, 2000).

ACCEPTED MANUSCRIPT

4.2 *Trench interpretation*

The detailed analysis of the trench walls provided evidence for four faulting events, characterized by normal sense of displacement. The recognition of the past faulting events was mainly based on sedimentological and crosscutting relationships observed in the fault zone. The stratigraphic sequences exposed by the trenches have been displaced and dragged by the main fault and its secondary splays in the downthrown fault block (Figs. 3–5).

The recognition of the most recent displacement event (E1) and the penultimate displacement event (E2) was based on the presence of filled fissures created on the base of the fault scarp during surface faulting. McCalpin (2005) proposed a conceptual model (*fissure-graben model*) of how fissure fills are formed during faulting events. According to this model, the surface faulting event creates a fissure at the base of the coseismic scarp which then fills with scarp-derived material from the free face and from the sides of the fissure. The downthrown fault block is then buried by graben aggradation and then follows surface stabilization and soil formation.

The stratigraphic evidence of the most recent surface faulting event (E1) is given by the youngest fissures fill deposits exposed in both trenches (Figs. 3-5). In trench G1 event E1 displaced and dragged units 2 and 3, and was immediately followed by the deposition of unit 7. Thus, the stratigraphic contact between units 6 and 7 would then correspond to the "event horizon" (*sensu* Pantosti et al., 1993) i.e. the ground surface at the time of event E1 (EH 1 in Fig. 3). Event E1 was responsible for a vertical displacement of about 0.60 m, measured from the thickness of unit 7, which is in agreement with the topographic offset of 0.60 m measured above the fault zone (Fig. 3). In addition, in trench G2, event E1 displaced and dragged along the main fault plane by 0.60 m the base of sub-unit 2b and is in agreement with the displacement estimated in trench G1. The fissure fill deposit (f1) observed in trench G2 was covered by the deposition of the upper part of unit 5. It was not possible to distinguish with confidence the stratigraphic contact between the upper and the lower part of unit 5 due to its massive and clayey nature and the pervading bioturbation, typical of a floodplain

ACCEPTED MANUSCRIPT

environment within abandoned meanders. Considering that the fissure fill must be located at the base of the co-seismic free face, the approximate position of the pre-faulting surface was possibly close to the upper part of the fissure fill. According to such an interpretation the approximate position of the pre-faulting surface, i.e. the event horizon of the event E1 (EH1), was drawn as a dash-dotted line in Fig. 4. For the sake of simplicity, we labeled the upper part of unit 5 as sub-unit 5c. In the same way, the previous assumptions were used elsewhere in this study.

The penultimate surface faulting event (E2) is recognized by the deposition of the second (older) fissure fill (f2) deposit in both of the two excavated trenches (Figs. 3 and 4). In trench G1, the fissure fill (f2) deposited after the faulting event E2 and was subsequently covered by the deposition of the upper part of unit 6 (sub-unit 6b). Sub-unit 6b represents the interseismic graben fill deposited between events E2 and E1. Consequently, the base of sub-unit 6b corresponds to the event horizon (EH2 in Fig. 3). The approximate position/shape of the event horizon E2 was drawn in Fig. 3 in a similar way as the event horizon E1. The lower part of unit 6 (sub-unit 6a) was deposited after a previous event (E3) and before the event E2 (Fig. 3). In trench G2 event E2 displaced and dragged units 2, 4 and the lower part of unit 5 (sub-unit 5a) along the southern secondary fault plane (Fig. 4). The middle part of unit 5 (sub-unit 5b) most likely was deposited shortly after the faulting event E2. Event horizon E2 in trench G2 may be placed, similar to event horizon E2 in trench G1, close to the top of the older fissure fill (f2). The vertical displacement during the surface faulting event E2 could not be estimated using offset stratigraphic units. However, in trench G2 a cumulative vertical displacement of 1.70 m was measured from the vertical offset of the top of sub-unit 2b. Subtracting the event E1 displacement (0.60 m) and the event E3 minimum displacement (0.50 m, discussed in the next paragraph), yields a value of 0.60 m for the event E2. However, this displacement value could be minimum because offset units were affected by near-fault drag.

An earlier surface faulting event (E3) was recognized within trench G1, as unit 5 was displaced by the southernmost secondary fault (Fig. 3), which was subsequently sealed by the

ACCEPTED MANUSCRIPT

deposition of the lower part of unit 6 (sub-unit 6a). We measured 0.5 m of vertical, down-to-the-south stratigraphic displacement using the top of unit 5, for this event. However, this displacement value could be minimum because the top of unit 5 probably experienced some erosion after the faulting event. In trench G2, during the event E3, units 2 and 4 were displaced and dragged along the southern secondary fault plane (Fig. 4). The lower part of unit 5 (sub-unit 5a) was subsequently deposited after the event E3. The event horizon E3 may be placed at the top of unit 4 (Figs. 4 and 5).

A fourth faulting event (E4) was defined on the basis of the scarp-derived colluvial deposit unit 4 observed in the trench G2 (Figs. 4 and 5). Event E4 occurred before the deposition of unit 4.

The studied trenches, along the GF, expose evidences of fissure fill deposits, scarp derived colluviums, angular unconformities in the downthrown fault block stratigraphy and absence of any paleosoil horizons. Hence, the structural and stratigraphic indications in the two trenches imply that the GF scarp is the result of episodic displacement accompanied by continuous deposition without soil formation in the downthrown fault block (McCalpin, 2003; McCalpin et al., 2011).

4.3 *Timing of the events*

OSL ages summarized in Table 2 constrain the ages of the four faulting events (E1, E2, E3 and E4) identified in the two trenches (Figs. 3-5). The most recent surface faulting event E1 is constrained by one maximum limiting age and by two minimum limiting ages. In trench G1 the base of unit 7 yielded an OSL age of 1.42 ± 0.06 ka (Gyr1OSL_10) and provides a minimum age of this event (Table 2; Fig. 3). In trench G2 the age of the "inductive" event horizon (EH1 in Fig. 4) was inferred from the OSL age of the samples Gyr2OSL_09E and Gyr2OSL_08E. Hence, the age of the "inductive" event horizon E1 in trench G2 is bracketed by a maximum age of 2.16 ± 0.03 ka and a minimum age of 1.35 ± 0.02 ka. Consequently, based on the dates from the two trenches, the event E1 occurred after 2.16 ± 0.03 ka and before 1.42 ± 0.06 ka (age of unit 7, trench G1). This event could be

ACCEPTED MANUSCRIPT

possibly related to a historical event that occurred between *ca* 2nd-1st century BC with a possible magnitude 6.0-6.5 (Caputo and Helly, 2005b). This historical event was recognized on the basis of archaeological and architectural evidences from Larissa and from nearby towns. Although, the authors stated as possible source of this event the Rodia Fault, we cannot exclude the GF.

Event E2 corresponds to the penultimate event is observed in both trenches and it is constrained by four maximum limiting ages and by two minimum limiting ages. In trench G1 the pottery sample Gyr1OSL_15 from the lower part of unit 6 (sub-unit 6a) provides an OSL age of 3.77 ± 0.13 ka representing a maximum age of this event (Table 2; Fig. 3). In trench G2 two samples (Gyr2OSL_05E and 06E) were dated from sub-unit 5a and provided OSL ages of 3.48 ± 0.07 ka and 3.77 ± 0.06 ka, respectively. On the other hand, a similar OSL age (3.64 ± 0.12 ka) was provided from a sample (Gyr2OSL_04E in Fig. 4) collected from the part of unit 5 situated between the main fault plane and the secondary fault. This similarity of ages allowed the hypothesis that sub-unit 5a was faulted and displaced along the secondary fault plane during the penultimate event (E2). Accordingly, these ages provide a maximum limiting age for the event E2. Further support for this hypothesis comes from the buried pottery found in trench G1 (Fig. 3) inside the lower part of unit 6 (sub-unit 6a). The minimum age of the event E2 is constrained by samples Gyr2OSL_08E and Gyr2OSL_07E from sub-unit 5b providing OSL ages of 2.16 ± 0.03 ka and 2.80 ± 0.06 ka, respectively (Table 2; Fig. 4). Thus, the second event occurred sometime after 3.77 ± 0.06 ka and before 2.16 ± 0.03 ka – 2.80 ± 0.06 ka, most likely before 2.80 ± 0.06 ka.

The maximum age of event E3 is constrained from sample Gyr2OSL_01W derived from unit 4 (trench G2) yielding an OSL age of 5.59 ± 0.13 ka (Table 2; Fig. 5). The minimum age is defined by the above discussed ages from sub-unit 6a in trench G1 and sub-unit 5a in trench G2 (Figs. 3 and 4). Therefore, the third event occurred sometimes after 5.59 ± 0.13 ka (unit 4, Fig. 5) and before 3.77 ± 0.06 ka (sub-units 6a and 5a, Figs. 3 and 4).

We have only one sample from trench G2 defining the minimum time limit of the fourth faulting event (E4). Based on the obtained OSL age of unit 4, it appears that the event

ACCEPTED MANUSCRIPT

E4 occurred before 5.59 ± 0.13 ka (Gyr2OSL_01W, Table 2), which provides the minimum age of this event (Figs. 4 and 5).

4.4 *Displacement per event and magnitude*

The vertical displacements for the paleoearthquakes E1, E2 and E3, as estimated stratigraphically from the two trenches, are 0.60, 0.60 and 0.50 m, respectively showing remarkable similarity in size. This implies that GF may display a "characteristic earthquake" behavior (Schwarz and Coppersmith, 1984). For this reason, we assumed a vertical displacement of 0.50–0.60 m also for the paleoearthquake E4. Following empirical relationships between magnitude and maximum vertical displacement (Wells and Coppersmith, 1994) and assuming the vertical displacement of 0.60 m per event that was observed in our trenches as maximum; we can calculate a moment magnitude (Mw) of the order of 6.5. By the same token, a moment magnitude of 6.5 is consistent with a surface rapture length of 18–19 km, which is longer than the mapped length of the GF. However, it is possible that inherited NW-SE trending extensional structures may be locally or partially reactivated with oblique kinematics (e.g., Caputo, 1993b).

We constructed two perpendicular topographic profiles, using a portable GPS receiver, across the surface trace of the fault directly east and west of the second trench (Fig. 2b). Each topographic profile exhibits breaks in slope, which are commonly related to "composite fault scarps" (*sensu* Stewart and Hanock, 1990), created by multiple faulting events (McCalpin, 2009b). We interpreted these inflections in slope mainly as the result of earlier faulting events rather than of erosional origin, on the basis of the multiple faulting events observed in the excavated trenches. The profile indicates a scarp height of 12 m, with a width of 120 - 130 m, and a maximum scarp-slope angle of *ca.* 7°. The cumulative surface offset is 12 m, based on original surfaces. This value is a first-order estimate of the cumulative vertical displacement. The vertical displacement for the three most recent events is well constrained and similar. The cumulative vertical displacement for these events, as

ACCEPTED MANUSCRIPT

obtained from trench G2, is 1.70 m. Accordingly, the 12 m-high scarp could be the result of as many as twenty linear morphogenic earthquakes.

4.5 *Recurrence interval and slip rate*

Although the timing of the three most recent events (E1, E2 and E3) is not very well constrained due to the massive character of the units 6 and 5 in trenches G1 and G2, respectively, we assumed that two complete earthquake cycles have occurred between 5.59 ± 0.13 ka (maximum age of event E3) and 1.42 ± 0.06 ka (minimum age of event E1). In order to calculate the apparent closed-cycle recurrence interval for each earthquake cycle (McCalpin, 2009c), we assumed that the most probable time of faulting is the mean between the minimum and the maximum limiting age for each event. Hence, the closed-cycle recurrence interval between events E2 (3.29 ± 0.07 ka) - E1 (1.79 ± 0.07 ka) and E3 (4.68 ± 0.09 ka) - E2 are 1.50 ± 0.10 ka and 1.40 ± 0.12 ka, respectively. A very similar average recurrence interval of 1.39 ± 0.14 ka may be calculated considering that the three events (E1, E2 and E3) occurred in the time span between 1.42 ± 0.06 ka and 5.59 ± 0.13 ka.

Three different apparent slip rate estimates were calculated for this study, based on interseismic intervals between the E2–E1, E3-E2, and E3-E1 events. The E2–E1 cycle slip rate, based on the most recent event vertical displacement of 0.60 m and a closed-cycle interval of 1.50 ± 0.10 ka, is 0.40 ± 0.03 mm/a. The E3-E2 cycle slip rate, based on the penultimate event vertical displacement of 0.60 m and a closed-cycle interval of 1.40 ± 0.12 ka is 0.43 ± 0.04 mm/a. The E3-E1 average slip rate, based on the cumulative vertical displacement of 1.70 m and the interseismic time interval of 4.17 ± 0.14 ka (between the maximum age of event E3 and the minimum age of event E1), is 0.41 ± 0.01 mm/a.

4.6 *Comparison with Tyrnavos and Rodia faults*

The first seismotectonic investigations to geologically identify past earthquakes within the Tyrnavos Basin were conducted along the Tyrnavos Fault (Caputo, 1993b; Caputo et al., 2004), where evidence for at least 12-13 earthquakes during the last 25-30 ka and a

ACCEPTED MANUSCRIPT

mean recurrence interval of 2-2.5 ka were reported. At least two of the earthquake events that were recognized in the excavated trenches occurred the last 7-8 ka BP. The mean co-seismic vertical displacement was estimated between 20 and 40 cm. Taking into account the location of the excavated trenches close to the eastern sector of the fault, these values probably represent 60-70% of the real throw (Caputo et al., 2004). Based on displaced alluvial deposits, boreholes and paleoseismologic data, a long-term slip rate ranging between 0.1 and 0.4 mm/a was suggested, while based on empirical relationships, the estimated maximum magnitude is 6.3-6.5 (Caputo, 1993b; Caputo et al., 2004; 2006).

Morphotectonic, structural, remote sensing and paleoseismological investigations were carried out also on the Rodia Fault (Caputo, 1993a; Caputo and Helly, 2005a), clearly documenting a Late Pleistocene to Holocene activity with a slip rate roughly ranging between 0.1 and 1.0 mm/a (class B following the RGAFJ, 1992). In particular, the last earthquake is dated 2-3 ka BP associated with a vertical displacement of 25-30 cm and a possible magnitude of 6.4 ± 0.2 (Caputo and Helly, 2005a).

Comparing our results with those from the antithetic Tyrnavos Fault and the synthetic right-stepping Rodia Fault, the GF seems characterized by a longer recurrence interval and slightly larger co-seismic vertical displacements. The estimated slip rate and the maximum possible magnitude are however comparable to those reported for the other investigated faults of the Tyrnavos Basin.

5. Concluding remarks

Although paleoseismological trenching can provide insight for the past behavior of seismogenic faults, the interpretation is not always straightforward. This is due to the difficulties in stratigraphic interpretations, especially for sites where sedimentary deposits of the downthrown fault block are under the influence of fluvial processes. Using a combination of OSL dating and paleoseismological trenching, we have estimated the timing of the observed paleoarthquakes related with the Gyrtoni Fault. The two paleoseismological

ACCEPTED MANUSCRIPT

trenches provide evidence of at least three, and possibly four faulting events (with ages ranging 2.16-1.42 ka, 3.77-2.80 ka, 5.59-3.77 ka, and <5.59 ka). Average recurrence interval (1.39 ± 0.14 ka) and slip rate (0.41 ± 0.01 mm/a) for the Gyrtoni Fault are in good agreement with the estimated closed-cycle recurrence intervals (1.50 ± 0.10 and 1.40 ± 0.12 ka) and closed-cycle slip rates (0.40 ± 0.03 and 0.43 ± 0.04 mm/a), respectively. In addition, a refined chronostratigraphy for the floodplain deposits exposed on the upthrown fault block was established.

Considering the possible time window (2.16-1.42 ka) of the last event (E1), it is noteworthy that the elapsed time is close to or could have exceeded the estimated recurrence interval values for the GF.

Since, the seismic history of northern Thessaly in general and specifically of the Gyrtoni Fault was not completely known our results improve the existing knowledge on the Holocene seismotectonics of the region. The outcome of the present study can be useful for the better assessing of the seismic hazard of the broader area.

Acknowledgements

This research project was implemented within the framework of the Action «Supporting Postdoctoral Researchers» of the Operational Program "Education and Lifelong Learning" and is co-financed by the European Social Fund (ESF) and the Greek State. The authors wish to thank A. Belesis, E. Kremastas and D. Kalyvas for their help and support during the field work. We would also like to thank Navin Juyal, Gabriel González and Editor-in-Chief Kelin Wang for their constructive comments that helped to improve the manuscript.

ACCEPTED MANUSCRIPT

References

Adamiec, G., Aitken,M.J., 1998. Dose-rate conversion factors: update. Ancient TL 16, 37–49.

Aitken, M. J., 1985. Thermoluminescence dating, Academic Press, London.

Ambraseys, N.N., Jackson, J.A., 1990. Seismicity and associated strain of central Greece between 1890 and 1988. Geophysical Journal International 101, 663–708.

Bailey, R.M., Smith, B.W., Rhodes, E.J., 1997. Partial bleaching and the decay form characteristics of quartz OSL. Radiat. Meas. 27, 123–136.

Barnett, M., 2000. Luminescence dating of pottery from Later Prehistoric Britain. Archaeometry 42 (2), 431-457.

Bøtter-Jensen, L., Andersen, C.E., Duller, G.A.T., Murray, A.S., 2003. Developments in radiation, stimulation and observation facilities in luminescence measurements. Radiation Measurements 37, 535-541.

Bøtter-Jensen, L., Thomsen, K. J. & Jain, M. 2010. Review of optically stimulated luminescence (OSL) instrumental developments for retrospective dosimetry. Radiation Measurements 45, 253–257.

Bronk Ramsey, C., 1995. Radiocarbon calibration and analysis of stratigraphy: the OxCal program. Radiocarbon 37 (2), 425–430.

Bronk Ramsey, C., 2001. Development of the radiocarbon calibration program OxCal. Radiocarbon 43 (2A), 355–363.

Caputo, R., 1990. Geological and structural study of the recent and active brittle deformation of the Neogene-Quaternary basins of Thessaly (Greece). In: Scientific Annals, Vol. 12, Aristotle University of Thessaloniki, Thessaloniki.

Caputo, R., 1993a. The Rodia Fault: an active complex shear zone (Larissa Basin, Central Greece). Bulletin of Geological Society of Greece XXVII, 447– 456.

Caputo, R., 1993b. Morphotectonics and kinematics along the Tyrnavos Fault, northern Larissa Plain, mainland Greece. Zeitschrift für Geomorphologie 94, 167–185.

ACCEPTED MANUSCRIPT

Caputo, R., 1995. Inference of a seismic gap from geological data: Thessaly (Central Greece) as a case study. Annali di Geofisica 38, 1–19.

Caputo, R., 2005. Ground effects of large morphogenic earthquakes. Journal of Geodynamics 40, 113–118.

Caputo, R., Pavlides, S., 1993. Late Cainozoic geodynamic evolution of Thessaly and surroundings (central-northern Greece). Tectonophysics 223, 339–362.

Caputo, R., Helly, B., 2005a. The Holocene activity of the Rodia Fault, Central Greece. Journal of Geodynamics. 40 (2–3), 153–169.

Caputo, R., Helly, B., 2005b. Archaeological evidences of past earthquakes: a contribution to the SHA of Thessaly, Central Greece. Journal of Earthquake Engineering 9(2), 199–222.

Caputo, R., Bravard, J.-P., Helly, B., 1994. The Pliocene–Quaternary tecto-sedimentary evolution of the Larissa Plain (Eastern Thessaly, Greece). Geodynamica Acta 7, 57–85.

Caputo, R., Helly, B., Pavlides, S., Papadopoulos, G., 2004. Palaeoseismological investigation of the Tyrnavos Fault (Thessaly Central Greece). Tectonophysics 394, 1–20.

Caputo, R., Helly, B., Pavlides, S., Papadopoulos, G., 2006. Archaeo- and palaeoseismological investigations in Northern Thessaly (Greece): Insights for the seismic potential of the region. Natural Hazards 39, 195-212.

Caputo, R., Sboras, S., Pavlides, S., Chatzipetros, A., 2015. Comparison between *single-event effects* and *cumulative effects* for the purpose of seismic hazard assessment. A review from Greece. Earth-Science Reviews 148, 94–120.

Caputo, R., Piscitelli, S., Oliveto, A., Rizzo, E. and Lapenna,V., 2003. The use of electrical resistivity tomography in Active Tectonic. Examples from the Tyrnavos Basin, Greece, Journal of Geodynamics 36 (1–2), 19–35.

Chatzipetros, A., Pavlides, S., Mountrakis, D., 1998. Understanding the 13 May 1995 western Macedonia earthquake: a paleoseismological approach. Journal of Geodynamics 26, 327–339.

ACCEPTED MANUSCRIPT

Chatzipetros, A., Kokkalas, S., Pavlides, S., Koukouvelas, I.K., 2005. Palaeoseismic data and their implication for active deformation in Greece. Journal of Geodynamics 40, 170–188.

Chen, Y.G., Chen, Y.W., Chen, W.S., Zhang, J.F., Zhaoc, H., Zhou, L.P., Li, S.H., 2003. Preliminary results of long-term slip rates of 1999 earthquake fault by luminescence and radiocarbon dating. Quaternary Science Reviews 22, 1213–1221.

Constantin, D., Begy, R., Vasiliniuc, S., Panaiotu, C., Necula, C., Codrea V., Timar-Gabor, A., 2014. High-resolution OSL dating of the Costines, ti section (Dobrogea, SE Romania) using fine and coarse quartz. Quaternary International 334-335, 20-29.

Demitrack, A., 1986. The Late Quaternary geologic history of the Larissa Plain, Thessaly, Greece: Tectonic, Climatic and Human Impact on the Landscape. Ph .D. dissertation, Stanford University, CA. Ann Arbor, Michigan: University Microfilms.

Duller, G.A.T., 2003. Distinguishing quartz and feldspar in single grain luminescence measurements. Radiation Measurements 37, 161-165.

Duller, G.A.T., 2007. Assessing the error on equivalent dose estimates derived from single aliquot regenerative dose measurements. Ancient TL 25, 15-24.

Duller, G.A.T., 2015. The Analyst software package for luminescence data: overview and recent improvements. Ancient TL 33 (1), 35-42.

Durcan, J.A., Roberts, H.M., Duller, G.A.T., Alizai, A.H., 2010. Testing the use of range-finder OSL dating to inform field sampling and laboratory processing strategies. Quaternary Geochronology 5, 86–90.

Fattahi, M., Walker, R., Hollingsworth, J., Bahroudi, A., Nazari, H., Talebian, M., Armitage, S., Stokes, S., 2006. Holocene slip-rate on the Sabzevar thrust fault, NE Iran, determined using optically-stimulated luminescence (OSL). Earth and Planetary Science Letters 245 (3–4), 673–684.

Fattahi, M., Nazari, H., Bateman, M.D., Meyere, B., Sébrier, M., Talebian, M., Le Dortz, K., Foroutan, M., Ahmadi Givi, F., Ghorashi, M., 2010. Refining the OSL age of the last earthquake on the Dheshir fault, Central Iran. Quaternary Geochronology 5 (2–3), 286–292.

ACCEPTED MANUSCRIPT

Galanopoulos, A. G., 1950. "Die beiden schadenbringenden Beben von Larissa aus den Jahren 1892 und 1941," Sonderdruck aus 'Gerlands Beitrage zur Geophysik' 62, Heft 1, 27–38, Akademische Verlagsgesellschaft Geest und Portig K.-G., Leipzig C 1.

Galbraith, R.F., Roberts, R.G., 2012. Statistical aspects of equivalent dose and error calculation and display in OSL dating: an overview and some recommendations. Quaternary Geochronology 11, 1-27.

Galbraith, R.F., Roberts, R.G., Laslett, G.M., Yoshida, H., Olley, J.M., 1999. Optical dating of single and multiple grains of quartz from Jinmium rock shelter, northern Australia: part I, experimental design and statistical models. Archaeometry 41, 339-364.

Galli. P., Giaccio, B., Messina, P., Peronace, E., 2016. Three magnitude 7 earthquakes on a single fault in central Italy in 1400 years, evidence by new paleoseismic results. Terra Nova 28 (2), 146 – 154.

Ghinassi, M., Nemec, W., Aldinucci, M., Nehyba, S., Özaksoy, V., Fidolini, F., 2014. Plan form evolution of ancient meandering rivers reconstructed from longitudinal outcrop sections. Sedimentology 61 (4), 952-957.

Grützner, C., Schneiderwind, S., Papanikolaou, I., Deligiannakis, G., Pallikarakis, A., Reicherter., K., 2016. New constraints on extensional tectonics and seismic hazard in northern Attica, Greece: the case of the Milesi Fault. Geophysical Journal International 204 (1), 180-199. doi:10.1093/gji/ggv443.

HSA, 2011. Demographic and social characteristics of the Resident Population of Greece according to the 2011 Population - Housing Census revision of 20/3/2014. Hellenic Statistic Authority. Available at: http://www.statistics.gr/en/statistics/-/publication/SAM03/-, last accessed at 24 April 2016.

Huntley, D.J., Godfrey-Smith, D.I., Thewalt, M.L.W., 1985. Optical dating of sediments. Nature 313, 105-107.

IGME, 1985. Geological Map of Greece, Scale 1:50000, Sheets: Larissa, Gonni. Institute of Geology and Mineral Exploration, Athens.

ACCEPTED MANUSCRIPT

Jain, M., Botter-Jensen, L., Singhvi, A. K., 2003. Dose evaluation using multiple-aquilot quartz OSL: Test of methods and a new protocol for improved accuracy and precision, Radiation Measurements 37, 67‑80. Keller, E.A., Pinter, N., 2002. Active Tectonics: Earthquakes, Uplift and Landscape. Prentice Hall, New Jersey.

Kokkalas, S., Pavlides, S., Koukouvelas, I., Ganas, A., Stamatopoulos, L., 2007. Paleoseismicity of the Kaparelli fault (eastern Corinth Gulf): evidence for earthquake recurrence and fault behavior. Boll. Soc. Geol. Ital. (Ital. J. Geosci.) 126, 387–395.

Lafuente, P., Arlegui, L.E., Liesa, C.L., Simón, J.L., 2011. Paleoseismological analysis of an intraplate extensional structure: the Concud fault (Iberian Chain, eastern Spain). International Journal of Earth Science (Geol Rundsch) 100, 1713–1732.

McCalpin, J.P., 2003. Criteria for determining the seismic significance of sackungen and other scarp-like landforms in mountainous regions, *in* Hart, E.W., ed., Ridge-Top Spreading in California: Contributions Toward Understanding a Significant Seismic Hazard: California Geological Survey, CD 2003-05, 2 CD-ROMs.

McCalpin, J.P., 2005. Late Quaternary activity of the Pajarito fault, Rio Grande rift of northern New Mexico, USA. Tectonophysics 408, 213-236.

McCalpin, J.P., 2009a. Field techniques in paleoseismology. Terrestrial environments. In: McCalpin, J.P. (Ed.), Paleoseismology. Academic Press, San Diego, pp. 29–118.

McCalpin, J.P., 2009b. Paleoseismology in Extensional Tectonic Environments. In: McCalpin, J.P. (Ed.), Paleoseismology. Academic Press, San Diego, pp. 161–269.

McCalpin, J.P., 2009c. Application of Paleoseismic Data to Seismic Hazard Assessment and Neotectonic Research. In: McCalpin, J.P. (Ed.), Paleoseismology. Academic Press, San Diego, pp. 1–106.

McCalpin, J.P., Bruhn, R.L., Pavlis, T.L., Gutierrez, F., Guerrero, J., Lucha, P., 2011. Antislope scarps, gravitational spreading, and tectonic faulting in the western Yakutat microplate, south coastal Alaska. Geosphere 7(5), 1143-1158.

ACCEPTED MANUSCRIPT

Moro, M., Gori, S., Falcucci, E., Saroli, M., Galadini, F., Salvi, S., 2013. Historical earthquakes and variable kinematic behaviour of the 2009 L'Aquila seismic event (central Italy) causative fault, revealed by paleoseismological investigations. Tectonophysics 583, 131-144.

Murray, A.S., Wintle, A.G., 2000. Luminescence dating of quartz using an improved single-aliquot regenerative-dose protocol. Radiation Measurements 32, 57–73.

Murray, A.S., Olley, J.M., 2002. Precision and accuracy in the optically stimulated luminescence dating of sedimentary quartz. Geochronometria 21, 1‑16.

Murray, A.S., Funder, S., 2003. OSL dating of a Danish coastal marine deposit: a test of accuracy. Quaternary Science Reviews 22, 1177‑1183.

Murray, A.S., Wintle, A.G., 2003. The single aliquot regenerative dose protocol: potential for improvements in reliability. Radiation Measurements 37, 377–381.

Murray, A.S., Marten, R., Johnston, A., Martin, P., 1987. Analysis for naturally occurring radionuclides at environmental concentrations by gamma spectrometry. Journal of Radioanalytical and Nuclear Chemistry 115, 263–288.

Pavlides S., Caputo R., Sboras S., Chatzipetros A., Papathanasiou G., Valkaniotis S., 2010. The Greek catalogue of active faults and database of seismogenic sources. Bulletin of the Geological Society of Greece XLIII (1), 486-494.

Oliveto, A., Mucciarelli, M., Caputo, R., 2004. HVSR prospecting in multi-layered environments: An example from the Tyrnavos Basin (Greece). Journal of Seismology 8, 395–406.

Özkaymak, C., Sözbilir, H., Uzel, B., Serdar Aky Üz, H., 2011. Geological and paleoseismological evidence for late Pleistocene–Holocene activity on the Manisa fault zone,Western Anatolia. Turk. J. Earth Sci. 20. http://dx.doi.org/10.3906/yer-0906-18.

Palyvos, N., Pavlopoulos, K., Froussou, E., Kranis, H., Pustovoytov, K., Forman, S. L., Minos-Minopoulos, D., 2010. Paleoseismological investigation of the oblique-normal Ekkara ground rupture zone accompanying the M 6.7‑7.0 earthquake on 30 April 1954

ACCEPTED MANUSCRIPT

in Thessaly, Greece: Archaeological and geochronological constraints on ground rupture recurrence. Journal of Geophysical Research 115, B06301.

Pantosti, D., Schwartz, D. P., and Valensise, G., 1993. Paleoseismology along the 1980 surface rupture of the Irpina fault: Implications for earthquake recurrence in the southern Apennines, Italy. Journal of Geophysical Research 98, 6561–6577.

Papaioannou, I., 1988. I seismiki istoria tis Larisas kata to 18o kai 19o aiona [The seismic history of Larissa during the 18th and 19th centuries], Eleftheria Newspaper, August 7, 1988, Larissa [in Greek].

Papazachos, B.C., Papazachou, C., 1997. The Earthquakes of Greece. Editions ZITI, Thessaloniki.

Pavlides S., Caputo R., Sboras S., Chatzipetros A., Papathanasiou G., Valkaniotis S., 2010. The Greek catalogue of active faults and database of seismogenic sources, Bulletin of the Geological Society of Greece XLIII (1), 486-494.

Peng, J., Dong, Z.B., Fan, F.Q., Long, H., Liu, X.J., 2013. R package numOSL: numeric routines for optically stimulated luminescence. Ancient TL 31, 41–48.

Polymeris, G.S., Kiyak, N.G., Koul, D.K., Kitis, G., 2014. The Firing Temperature of Pottery from Ancient Mesopotamia, Turkey, Using Luminescence Methods: A Case Study for Different Grain-Size Fractions. Archaeometry 56 (5), 805–817.

Porat, N., Wintle, A.G., Amit, R., Enzel, Y., 1996. Late Quaternary earthquake chronology from luminescence dating of colluvial and alluvial deposits of the Arava Valley, Israel. Quaternary Research 46, 107–117.

Prescott, J.R., Hutton, J.T., 1994. Cosmic ray contribution to dose rates for luminescence and ESR dating: large depths and long-term time variations. Radiation Measurements 23, 497–500.

Reimer, P.J., Bard, E., Bayliss, A., Beck, J.W., Blackwell, P.G., Ramsey, C.B., Buck, C.E., Cheng, H., Edwards, R.L., Freidrich, M., Grootes, P.M., Guilderson, T.P., Haflidason, H., Hajdas, I., Hatt_e, C., Heaton, T.J., Hoffmann, D.L., Hogg, A.G., Hughen, K.A., Kaiser, K.F., Kromer, B., Manning, S.W., Niu, M., Reimer, R.W., Richards, D.A., Scott,

ACCEPTED MANUSCRIPT

E.M., Southon, J.R., Staff, R.A., Turney, C.S.M., van der Plicht, J., 2013. IntCal13 and marine13 radiocarbon age calibration curves 0-50.000 Years cal BP. Radiocarbon 55 (4), 1869-1887.

RGAFJ (Research Group for Active Faults of Japan), 1992. Maps of active faults in Japan with explanatory text. University of Tokyo Press, Tokyo, pp.73.

Rhodes EJ, Bronk-Ramsey C, Outram Z, Batt C, Willis L, et al. 2003. Bayesian methods applied to the interpretation of multiple OSL dates: high precision sediment age estimates from Old Scatness Broch excavations, Shetland Isles. Quaternary Science Reviews 22, 1231–44.

Schneider, H.A., 1968. Zur Quartargeologischen Entwicklungsgeschichte Thessaliens (Griechenland). R. Haber Verlag, pp. 127, 65 tabs., Berlin.

Schwartz, D.P., Coppersmith, K.J., 1984. Fault behavior and characteristic earthquakes: examples from the Wasatch and San Andreas Fault Zones. Journal of Geophysical Research 89 (B7), 5681–5698.

Singhvi, A. K., Sharma, Y. P., Agrawal, D. P., 1982. Thermoluminescence dating of dune sands in Rajasthan, India, Nature, 295, 313‑315.

Stewart, I.S, Hancock, P.L., 1990. What is a fault scarp?. Episodes, 13 (4), 256–263.

Stucchi M., Rovida A., Gomez Capera A.A., Alexandre P., Camelbeeck T., Demircioglu M.B., Gasperini P., Kouskouna V., Musson R.M.W., Radulian M., Sesetyan K., Vilanova S., Baumont D., Bungum H., Fäh D., Lenhardt W., Makropoulos K., Martinez Solares J.M., Scotti O., Živcic M., Albini P., Batllo J., Papaioannou C., Tatevossian R., Locati M., Meletti C., Viganò D., and Giardini D., 2013. The SHARE European Earthquake Catalogue (SHEEC) 1000-1899. Journal of Seismology, 17, 2, pp.524-544. doi: http://doi.org/10.1007/s10950-012-9335-2. Interactive catalogue available at: http://www.emidius.eu/SHEEC/sheec_1000_1899, last accessed at 24 April 2016.

ACCEPTED MANUSCRIPT

Trumbore, S.E., 2000. Radiocarbon geochronology. In: Noller, J.S., Sowers, J.M., Lettis, W.R. (Eds.), Quaternary Geochronology. American Geophysical Union, Washington, USA, pp. 41‑60.

van Andel, T.H., Zangger, E., Demitrack, A., 1990. Land use and soil erosion in prehistoric and historical Greece. J. Field Archaeology, 17, 379-376.

Vanneste, K., Radulov, A., De Martini, P., Nikolov, G., Petermans, T., Verbeeck, K., Camelbeeck, T., Pantosti, D., Dimitrov, D., Shanov, S., 2006. Paleoseismologic investigation of the fault rupture of the 14 April 1928 Chirpan earthquake (M 6.8), southern Bulgaria. J. Geophys. Res. 111, B01303.

Wallace, R. E., 1977. Profiles and ages of young fault scarps, north-central Nevada. Geological Society of America Bulletin 88, 1267–1281.

Wallinga, J., Murray, A., Wintle, A., 2000. The single-aliquot regenerative-dose (SAR) protocol applied to coarse grain feldspar. Radiation Measurements 32, 529–533.

Wells, D.L., Coppersmith, K.J., 1994. New empirical relationships among magnitude, rupture length, rupture width, rupture area, and surface displacement. Bulletin of the Seismological Society of America 84, 974–1002.

Zygouri, V., Koukouvelas, I.K., Kokkalas, S., Xypolias, P., Papadopoulos, G.A., 2015. The Nisi Fault as a key structure for understanding the active deformation of the NW Peloponnese, Greece, Geomorphology, 237**,** 142–156.

ACCEPTED MANUSCRIPT

Figures

Fig. 1. (a) Digital Elevation Model with hill-shading relief of the Tyrnavos Basin showing the main structural features (faults adopted from Caputo et al., 1994). Location of earthquakes epicenters (stars) compiled from SHEEC (1000-1899) interactive catalogue (Stucchi et al., 2012), Galanopoulos (1950), Papaioannou (1988), Ambraseys and Jackson (1990), Caputo (1995) and Papazchos and Papazchou (1997). (b) Simplified geological map (IGME, 1985; Caputo, 1990) of the study area, and the locations of the two trenches. Images taken form Google Earth.

Fig. 2. (a) Electric resistivity tomographies acquired across the Gyrtoni Fault with 10 m electrode spacing. Elevations in m a.s.l., resistivity in Ωm and RMS are 10.0 (GE1) and 20.5 (GE2). According to the two ERT, the fault trace is located at the base of the morphological escarpment. H: Holocene alluvial deposits; P: Late Pleistocene floodplane deposits; Tr: Triassic crystalline limestone (redrawn from Caputo et al., 2003). (d) Topographic profiles at the second trenching site located east (A'-A) and west (B'-B) of the trench G2. Profiles were surveyed perpendicular to the local surface trace of the fault scarp. SO: Surface offset. ERT profile locations are shown in Fig. 1. In both profiles, the vertical scale is different to the horizontal scale. Inset field view of the fault scarp from the west.

Fig. 3. Log of the east wall of trench G1 excavated across the fault scarp. OSL ages are expressed as thousands of years before 2014 AD. Radiocarbon dates are calibrated to calendar years and 64 years were added in order to give them the same reference point as the luminescence ages. Event horizons are marked with dotted and dashed lines and faults in red. (A) View of the trench from the north. (B) View of the east wall of the trench. (C) - (D) Close-up photographs showing the two fissure fills. (E) A close-up photograph showing the buried pottery. Trench location is shown in Fig. 1.

ACCEPTED MANUSCRIPT

Fig. 4. Log and photomosaic of the east wall of trench G2 excavated across the fault scarp. OSL ages are expressed as thousands of years before 2014 AD. Event horizons are marked with dotted and dashed lines and faults in red. Trench location is shown in Fig. 1.

Fig. 5. Log of the west wall of trench G2 excavated across the fault scarp. OSL ages are expressed as thousands of years before 2014 AD. Radiocarbon dates are calibrated to calendar years and 64 years were added in order to give them the same reference point as the luminescence ages. Event horizons are marked with dotted and dashed lines and faults in red. (A) View of the west wall of the trench. (B) A close-up photograph showing the fault zone. Trench location is shown in Fig. 1.

Fig. 6. Typical OSL decay curves (inset) and SAR growth curves for pottery (Gyr1OSL_13) and sediment (Gyr2OSL_07E and Gyr1OSL_06) samples using a 260 ^{o}C and 240 ^{o}C preheat for 10 s, respectively, and a 160 ^{o}C cut heat.

Fig. 7. Preheat plateau test results for sediment sample Gyr2OSL_07E (a) and pottery sample Gyr1OSL_13 (b) using eight different preheat temperatures held for 10s. Cut heat temperature was 160 ^{o}C and the test dose was 5 Gy. The dashed line represents the mean *De* obtained from the different preheat temperatures. (c - d) The corresponding recycling ratios and recuperation for each of the preheat temperatures for the same samples are also shown. The solid line indicates unity, whilst the dashed lines are located at ± 10%. Each data point represents the average of three aliquots and error bars show the standard deviation.

Fig. 8. Dose recovery test results for sediment sample Gyr2OSL_07E (a) and pottery sample Gyr1OSL_13 (b) and the variation of recycling ratios and recuperation (c - d) using eight different preheat temperatures held for 10s. Cut heat temperature was 160 ^{o}C and the test dose was 5 Gy. The solid line indicates unity, whilst the dashed lines are located at ±

ACCEPTED MANUSCRIPT

10%. Each data point represents the average of three aliquots and error bars show the standard deviation.

ACCEPTED MANUSCRIPT

ACCEPTED MANUSCRIPT

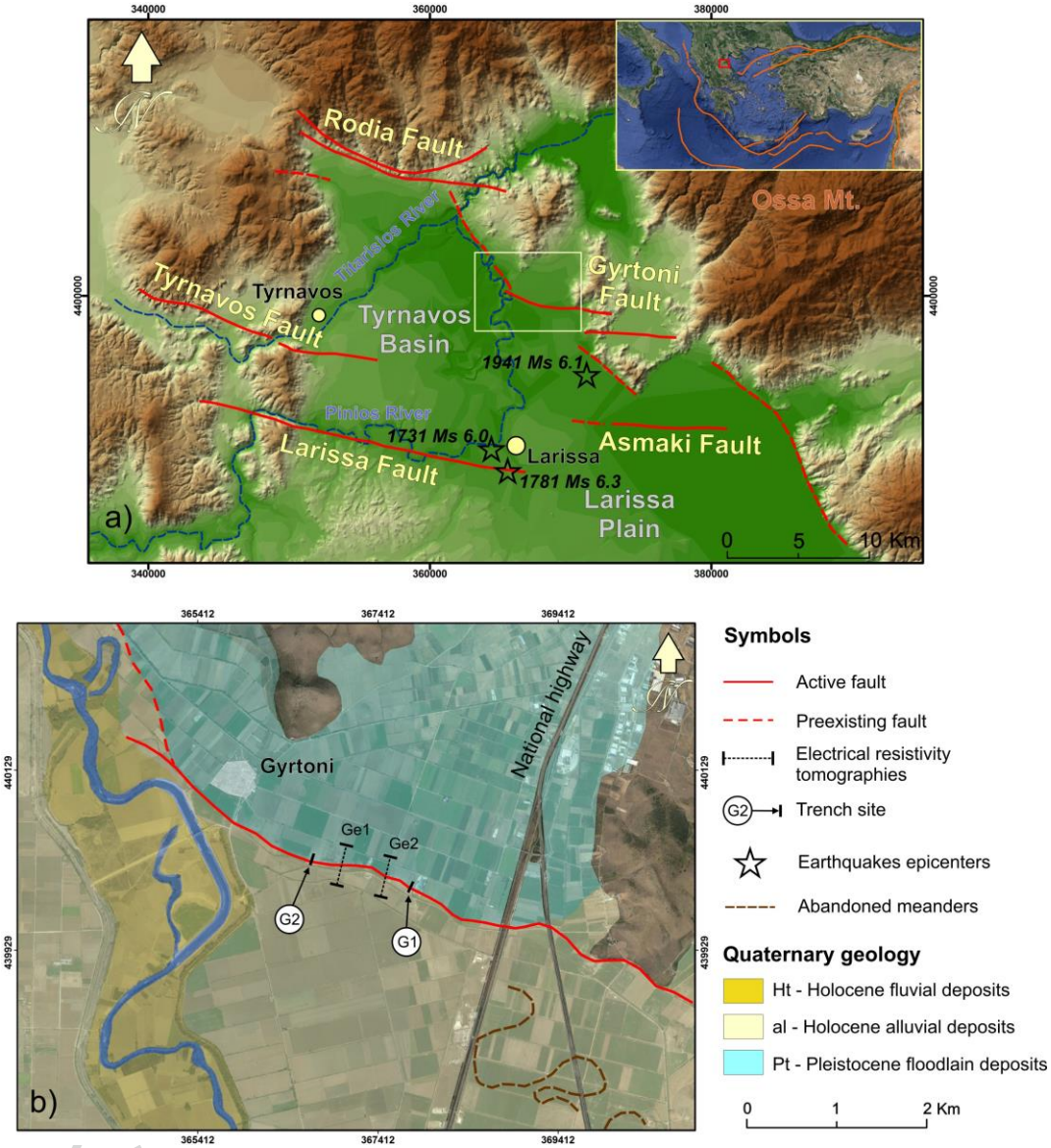

Fig. 1

ACCEPTED MANUSCRIPT

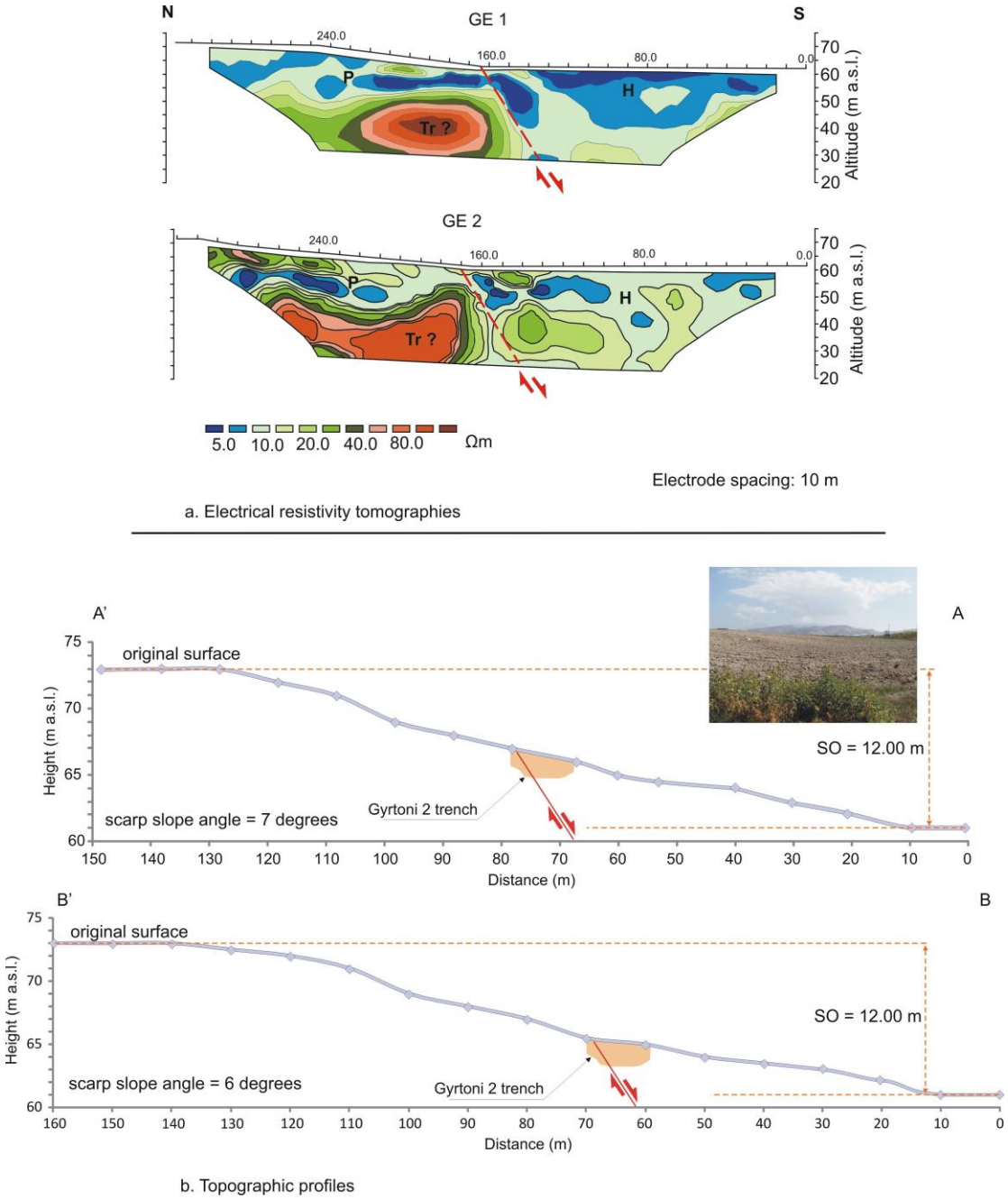

Fig. 2

ACCEPTED MANUSCRIPT

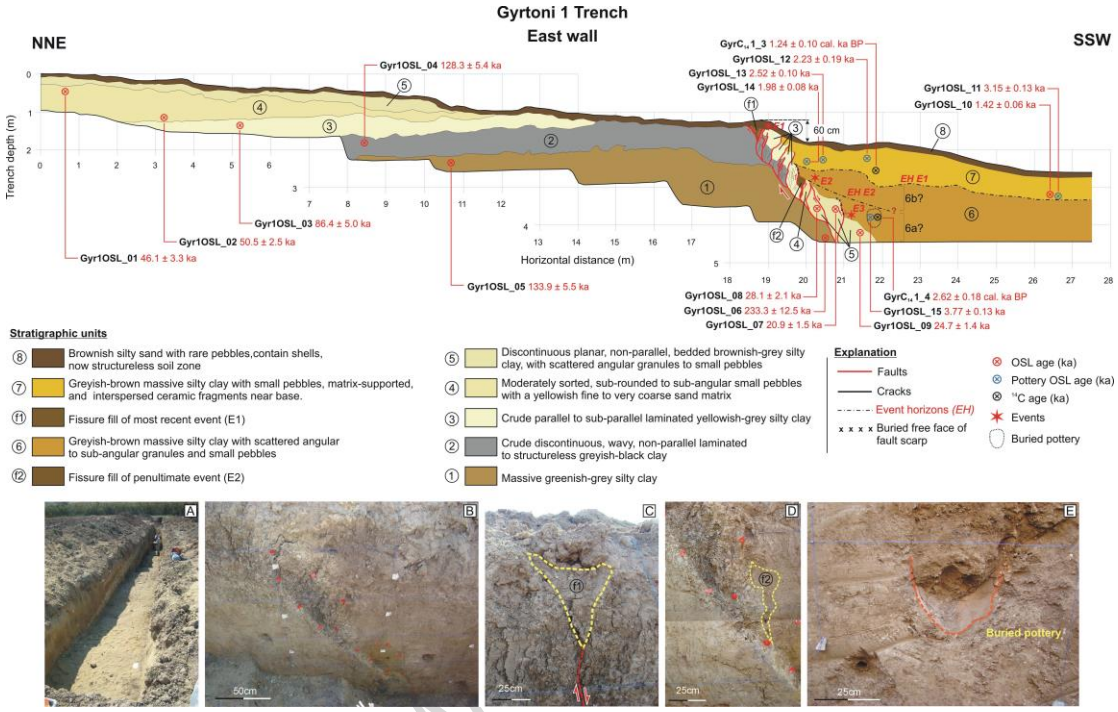

Fig. 3

ACCEPTED MANUSCRIPT

ACCEPTED MANUSCRIPT

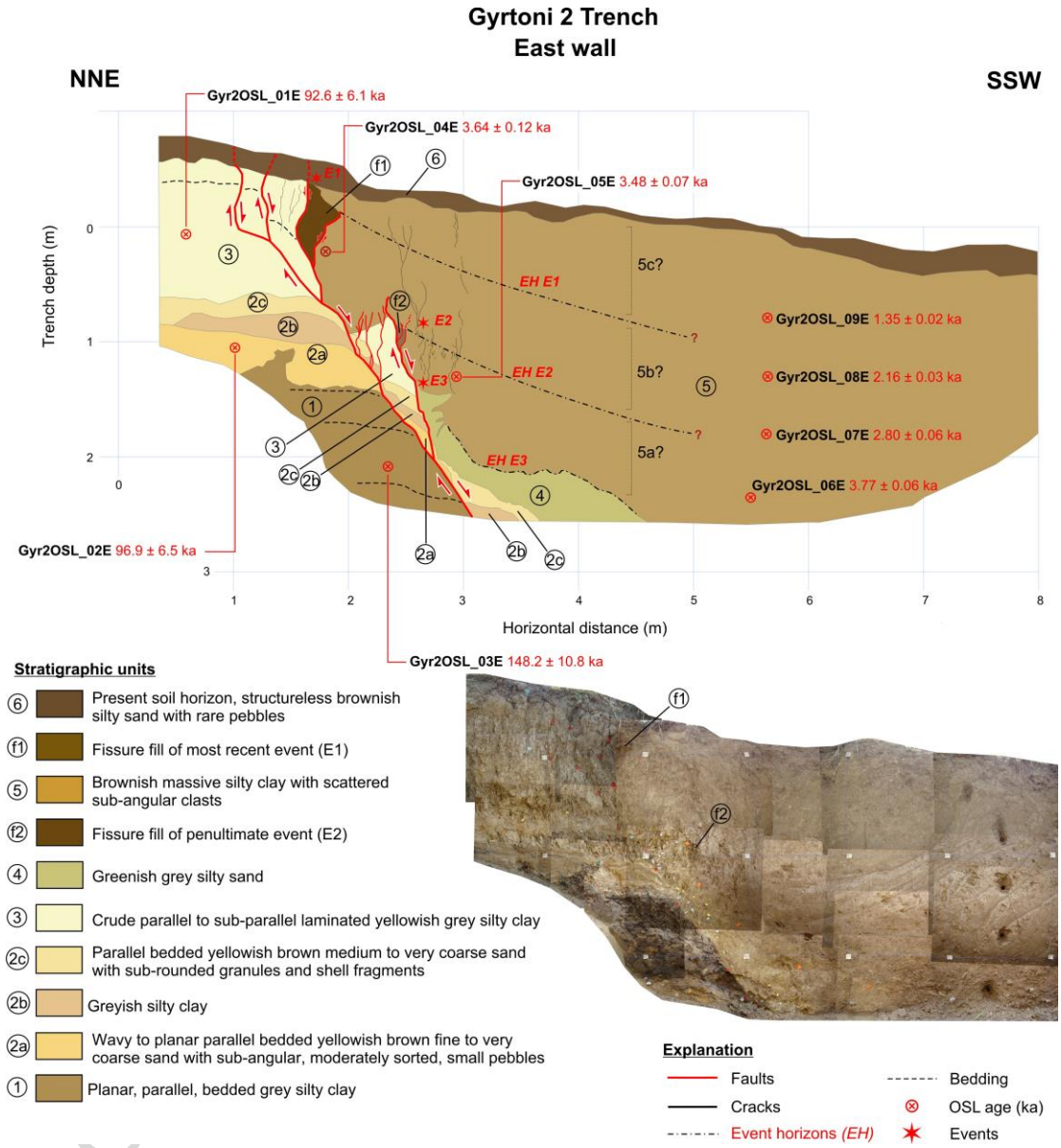

Fig. 4

ACCEPTED MANUSCRIPT

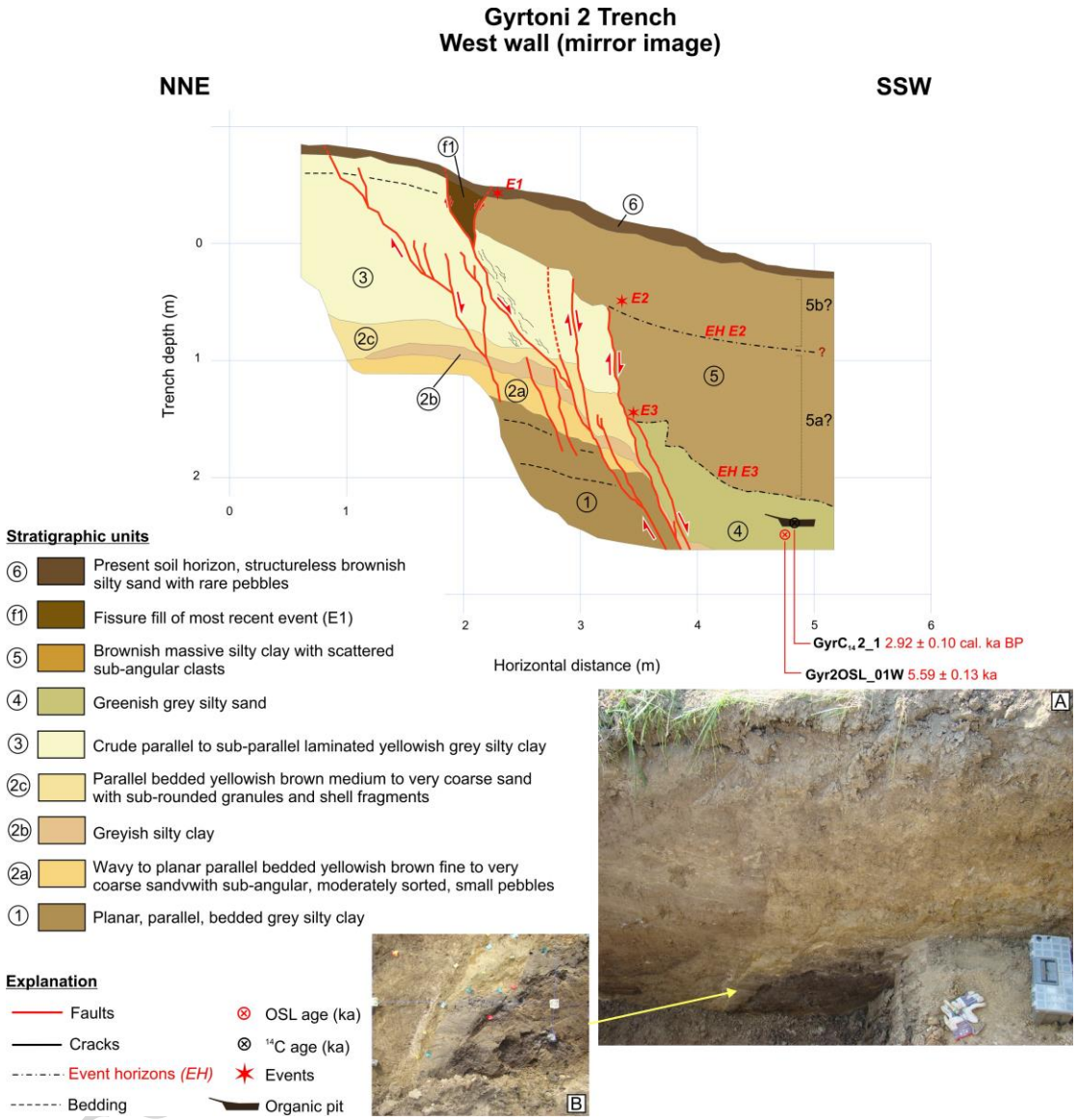

Fig. 5

ACCEPTED MANUSCRIPT

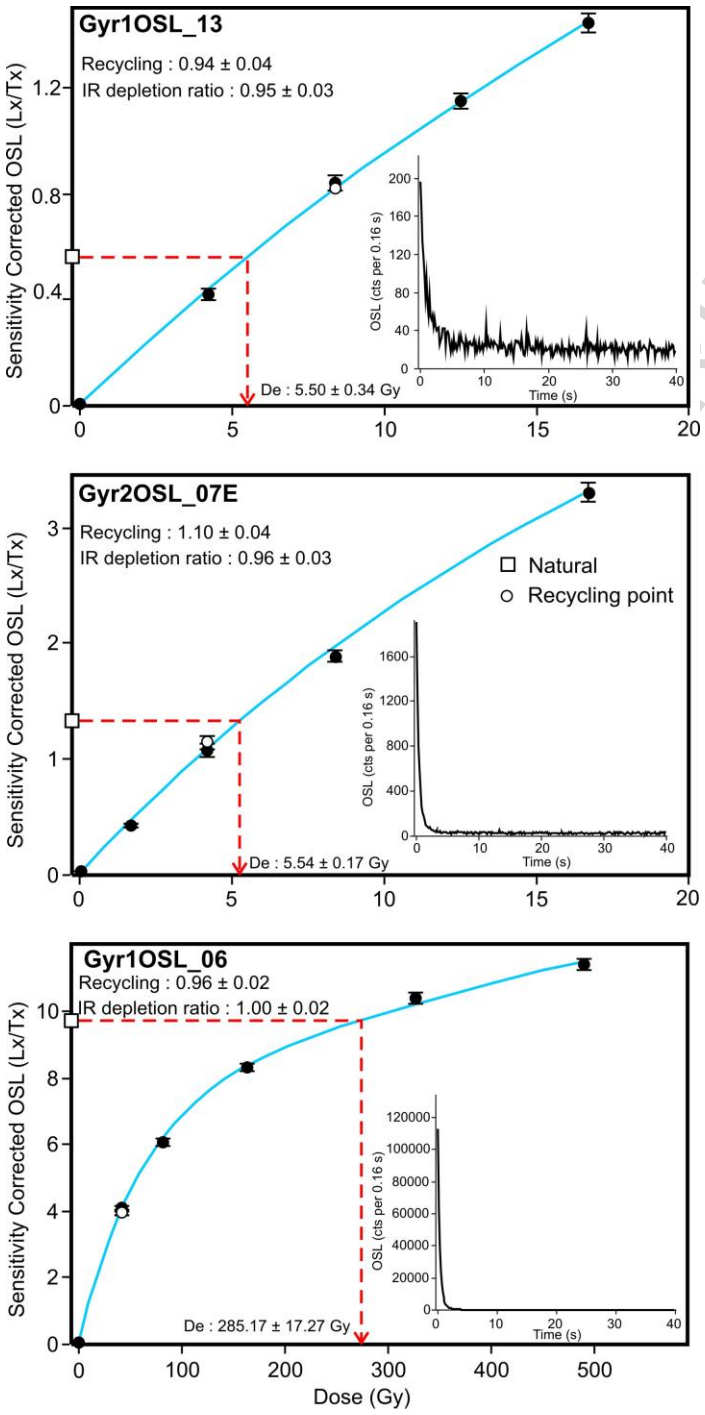

Fig.6

ACCEPTED MANUSCRIPT

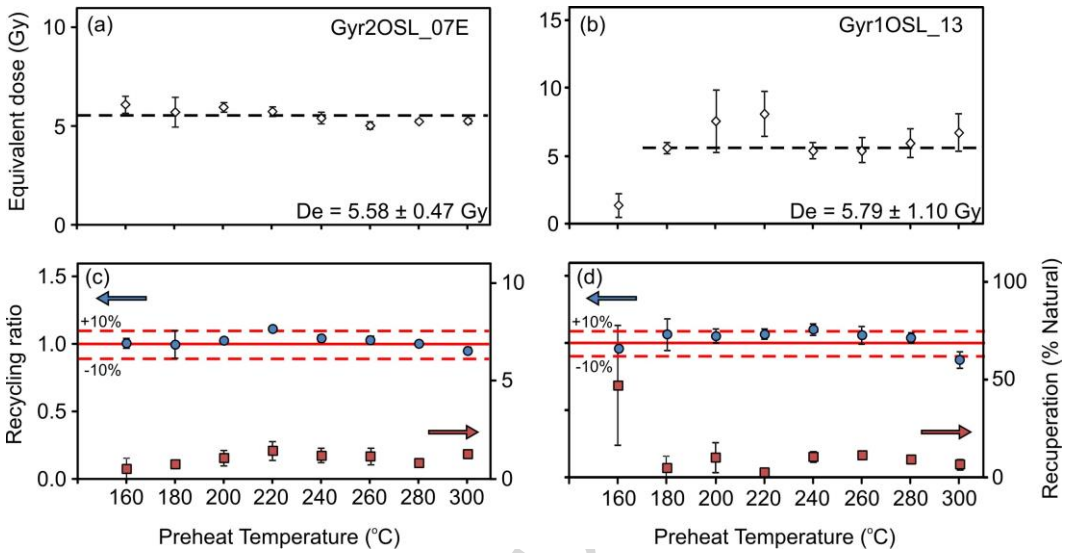

Fig. 7

ACCEPTED MANUSCRIPT

ACCEPTED MANUSCRIPT

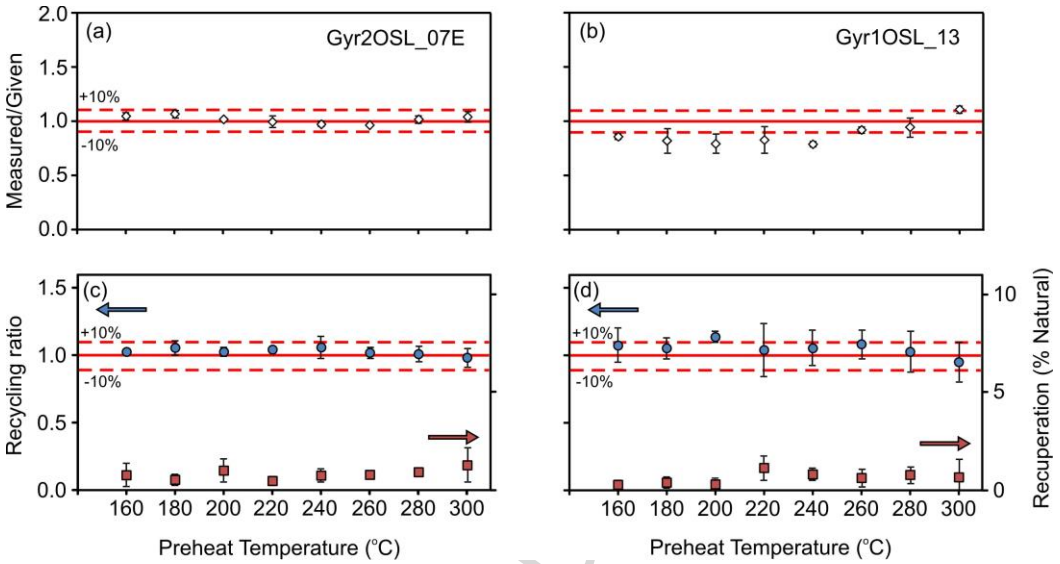

Fig. 8

ACCEPTED MANUSCRIPT

ACCEPTED MANUSCRIPT

Table 1

Sample information, radionuclide concentrations and dose rates results for luminescence samples collected from the two paleoseismological trenches at Gyrtoni Fault, Thesally, Central Greece.

Sample no.	Sample position	Material	Depth (m)[a]	Water Content (%)[b]	^{238}U (Bq/kg)[c]	^{232}Th (Bq/kg)[c]	^{40}K (Bq/kg)[c]	External β dose rate (Gy/ka)[d]	External γ dose rate (Gy/ka)[d]	Cosmic dose rate (Gy/ka)[e]	Total dose rate (Gy/ka)[f]
Gyrtoni 1 trench											
Gyr1OSL_01	Upthrown block	Sediment	0.5	7.3	28.1 ± 1.3	16.3 ± 1.1	327.8 ± 25.3	0.98 ± 0.05	0.65 ± 0.02	0.21 ± 0.02	1.84 ± 0.06
Gyr1OSL_02	Upthrown block	Sediment	1.1	5.5	20.2 ± 0.9	12.7 ± 0.7	279.5 ± 20.0	0.82 ± 0.04	0.52 ± 0.02	0.18 ± 0.02	1.51 ± 0.05
Gyr1OSL_03	Upthrown block	Sediment	0.7	19.2	38.1 ± 1.5	30.3 ± 1.5	489.9 ± 34.6	1.29 ± 0.06	0.89 ± 0.03	0.19 ± 0.02	2.37 ± 0.07
Gyr1OSL_04	Upthrown block	Sediment	1.2	26.6	24.5 ± 1.2	31.6 ± 1.4	454.6 ± 32.2	1.05 ± 0.05	0.73 ± 0.02	0.18 ± 0.02	1.96 ± 0.06
Gyr1OSL_05	Upthrown block	Sediment	1.4	23.6	26.2 ± 1.1	21.5 ± 1.1	347.2 ± 23.8	0.87 ± 0.04	0.60 ± 0.02	0.17 ± 0.02	1.64 ± 0.05
Gyr1OSL_06	Upthrown block	Sediment	2.5	43.7	20.4 ± 0.8	21.7 ± 0.8	269.3 ± 18.0	0.58 ± 0.03	0.43 ± 0.01	0.15 ± 0.02	1.17 ± 0.03
Gyr1OSL_07	Fault zone	Sediment	1.8	17.1	20.0 ± 1.1	23.3 ± 1.2	349.3 ± 27.6	0.89 ± 0.05	0.61 ± 0.02	0.17 ± 0.02	1.67 ± 0.06
Gyr1OSL_08	Fault zone	Sediment	1.8	12.2	15.0 ± 0.9	19.0 ± 1.1	445.0 ± 30.7	1.05 ± 0.06	0.62 ± 0.03	0.17 ± 0.02	1.84 ± 0.07
Gyr1OSL_09	Fault zone	Sediment	2.2	14.9	29.4 ± 1.3	20.4 ± 1.1	369.6 ± 27.3	1.01 ± 0.05	0.68 ± 0.02	0.16 ± 0.02	1.85 ± 0.06
Gyr1OSL_10	Downthrown block	Sediment	0.7	12.6	29.1 ± 1.4	28.8 ± 1.4	499.3 ± 34.3	1.32 ± 0.07	0.87 ± 0.03	0.20 ± 0.02	2.38 ± 0.07
Gyr1OSL_11	Downthrown block	Pottery	0.7	13.8	28.9 ± 1.3	26.0 ± 1.3	498.2 ± 35.7	1.28 ± 0.07	0.83 ± 0.03	0.20 ± 0.02	2.31 ± 0.08
Gyr1OSL_12	Downthrown block	Pottery	1.0	9.7	27.2 ± 1.4	30.0 ± 1.6	504.2 ± 35.9	1.36 ± 0.07	0.89 ± 0.03	0.18 ± 0.02	2.43 ± 0.08
Gyr1OSL_13	Downthrown block	Pottery	1.0	14.6	33.0 ± 1.5	26.5 ± 1.4	505.9 ± 35.2	1.32 ± 0.07	0.86 ± 0.03	0.18 ± 0.02	2.37 ± 0.07
Gyr1OSL_14	Downthrown block	Pottery	1.0	13.5	26.2 ± 1.1	25.4 ± 1.1	512.1 ± 31.1	1.29 ± 0.06	0.81 ± 0.03	0.18 ± 0.02	2.28 ± 0.07
Gyr1OSL_15	Downthrown block	Pottery	2.0	16.5	29.8 ± 1.1	25.0 ± 1.1	464.5 ± 30.1	1.19 ± 0.05	0.78 ± 0.02	0.16 ± 0.02	2.13 ± 0.06
Gyrtoni 2 trench-East wall											
Gyr2OSL_01E	Upthrown block	Sediment	0.9	13.9	19.3 ± 0.4	25.5 ± 0.6	330.5 ± 3.3	1.00 ± 0.01	0.63 ± 0.01	0.19 ± 0.02	1.81 ± 0.02
Gyr2OSL_02E	Upthrown block	Sediment	1.8	14.0	22.0 ± 0.4	32.2 ± 0.5	344.4 ± 4.6	1.03 ± 0.01	0.73 ± 0.01	0.17 ± 0.02	1.92 ± 0.02
Gyr2OSL_03E	Upthrown block	Sediment	2.4	47.3	37.6 ± 0.6	53.5 ± 0.8	359.3 ± 4.1	1.02 ± 0.01	0.81 ± 0.01	0.15 ± 0.02	1.98 ± 0.02
Gyr2OSL_04E	Downthrown block	Sediment	0.8	11.4	20.3 ± 0.4	28.2 ± 0.6	434.1 ± 3.7	1.26 ± 0.01	0.76 ± 0.01	0.19 ± 0.02	2.21 ± 0.02
Gyr2OSL_05E	Downthrown block	Sediment	1.6	16.3	24.6 ± 0.4	26.3 ± 0.6	418.6 ± 3.7	1.20 ± 0.01	0.72 ± 0.01	0.17 ± 0.02	2.09 ± 0.02
Gyr2OSL_06E	Downthrown block	Sediment	2.4	34.9	26.5 ± 0.5	27.1 ± 0.6	418.7 ± 3.8	1.02 ± 0.01	0.63 ± 0.01	0.15 ± 0.02	1.81 ± 0.02
Gyr2OSL_07E	Downthrown block	Sediment	1.8	15.1	20.8 ± 0.4	26.3 ± 0.6	404.4 ± 3.6	1.15 ± 0.01	0.69 ± 0.01	0.17 ± 0.02	2.01 ± 0.02
Gyr2OSL_08E	Downthrown block	Sediment	1.4	13.4	30.1 ± 0.5	31.2 ± 0.6	436.4 ± 3.8	1.35 ± 0.01	0.85 ± 0.01	0.18 ± 0.02	2.38 ± 0.02
Gyr2OSL_09E	Downthrown block	Sediment	0.9	13.1	20.5 ± 0.4	29.8 ± 0.6	482.4 ± 4.0	1.35 ± 0.01	0.79 ± 0.01	0.19 ± 0.02	2.33 ± 0.02
Gyrtoni 2 trench-West wall											
Gyr2OSL_01W	Downthrown block	Sediment	2.4	24.6	20.4 ± 0.4	28.3 ± 0.5	399 ± 3.5	1.04 ± 0.01	0.65 ± 0.01	0.16 ± 0.02	1.85 ± 0.02

[a] Depth below the surface of the trench.

[b] Water content expressed as a percentage of the mass of dry sediment, calculated using field values.

[c] Concentrations of ^{238}U, ^{232}Th and ^{40}K were determined from laboratory measurements using high-resolution gamma spectrometry.

[d] Beta and gamma dose rates were calculated using the conversion factors of Adamiec and Aitken (1998) and are shown rounded to two decimal places, although the total dose rates were calculated using values prior to rounding. Dose rates have been corrected for the effect of the water content and grain size.

[e] Cosmic dose rates were calculated according to Prescott and Hutton (1994).

ACCEPTED MANUSCRIPT

[f] Total dose rates were calculated after Aitken (1985).

ACCEPTED MANUSCRIPT

ACCEPTED MANUSCRIPT

Table 2
Equivalent doses (De) and quartz OSL ages calculated for samples collected from the two paleoseismological trenches at Gyrtoni Fault, Thesally, Central Greece.

Sample no.	Grain size (μm)	Aliquots (n)[a]	σ_{OD} (%)[b]	Total dose rate (Gy/ka)	Equivalent dose De (Gy)	Age (ka)[d]
					CAM[c]	CAM
Gyrtoni 1 trench						
Gyr1OSL_01	125 - 250	27	33	1.84 ± 0.06	84.91 ± 5.36	46.1 ± 3.3
Gyr1OSL_02	125 - 250	28	19	1.51 ± 0.05	76.54 ± 2.90	50.5 ± 2.5
Gyr1OSL_03	125 - 250	16	17	2.37 ± 0.07	204.85 ± 10.14	86.4 ± 5.0
Gyr1OSL_04	125 - 250	20	11	1.96 ± 0.06	250.95 ± 7.00	128.3 ± 5.4
Gyr1OSL_05	125 - 250	27	13	1.64 ± 0.05	220.08 ± 6.34	133.9 ± 5.5
Gyr1OSL_06	125 - 250	24	21	1.17 ± 0.03	273.14 ± 12.56	233.3 ± 12.5
Gyr1OSL_07	125 - 250	25	30	1.67 ± 0.06	34.77 ± 2.12	20.9 ± 1.5
Gyr1OSL_08	125 - 250	22	30	1.84 ± 0.07	51.68 ± 3.44	28.1 ± 2.1
Gyr1OSL_09	125 - 250	32	26	1.85 ± 0.06	45.74 ± 2.13	24.7 ± 1.4
Gyr1OSL_10	125 - 250	43	17	2.38 ± 0.07	3.38 ± 0.09	1.42 ± 0.06
Gyr1OSL_11	100 - 150	50	18	2.31 ± 0.08	7.26 ± 0.19	3.15 ± 0.13
Gyr1OSL_12	100 - 150	17	29	2.43 ± 0.08	5.42 ± 0.44	2.23 ± 0.19
Gyr1OSL_13	100 - 150	41	11	2.37 ± 0.07	5.96 ± 0.13	2.52 ± 0.1
Gyr1OSL_14	100 - 150	41	13	2.28 ± 0.07	4.52 ± 0.11	1.98 ± 0.08
Gyr1OSL_15	100 - 150	42	12	2.13 ± 0.06	8.03 ± 0.16	3.77 ± 0.13
Gyrtoni 2 trench-East wall						
Gyr2OSL_01E	63 - 100	23	29	1.81 ± 0.02	167.9 ± 10.8	92.6 ± 6.1
Gyr2OSL_02E	100 - 150	20	24	1.92 ± 0.02	186.5 ± 12.4	96.9 ± 6.5
Gyr2OSL_03E	63 - 100	10	21	1.98 ± 0.02	293.6 ± 21.2	148.2 ± 10.8
Gyr2OSL_04E	63 - 100	24	16	2.21 ± 0.02	8.04 ± 0.26	3.64 ± 0.12
Gyr2OSL_05E	63 - 100	26	9	2.09 ± 0.02	7.28 ± 0.14	3.48 ± 0.07
Gyr2OSL_06E	63 - 100	25	6	1.81 ± 0.02	6.83 ± 0.09	3.77 ± 0.06
Gyr2OSL_07E	63 - 100	25	8	2.01 ± 0.02	5.62 ± 0.1	2.8 ± 0.06
Gyr2OSL_08E	63 - 100	26	5	2.38 ± 0.02	5.13 ± 0.05	2.16 ± 0.03
Gyr2OSL_09E	63 - 100	26	7	2.33 ± 0.02	3.14 ± 0.05	1.35 ± 0.02
Gyrtoni 2 trench-West wall						
Gyr2OSL_01W	63 - 100	25	9	1.85 ± 0.02	10.31 ± 0.21	5.59 ± 0.13

[a] n is the number of aliquots accepted for De calculations.
[b] σ_{OD} is the overdispersion of the De distribution.
[c] Equivalent doses (De) and OSL ages calculated using the central age model (CAM) of Galbraith et al. (1999).
[d] OSL ages are expressed as thousands of years (ka) before 2014 AD, and rounded to the nearest 100 years with the exception of the relatively young samples which are rounded to the nearest 10 years.

ACCEPTED MANUSCRIPT

Highlights

- Two paleoseismological trenches were excavated across the Gyrtoni Fault
- OSL dating using the SAR protocol constrained the timing of the past earthquakes
- Three surface faulting events occurred the last 5.59 ± 0.13 ka
- An average fault slip rate of 0.41 ± 0.01 mm/a was estimated
- An average recurrence time of 1.39 ± 0.14 ka was estimated

ACCEPTED MANUSCRIPT